Department of Physics and Astronomy

University of Heidelberg

Master thesis

in Physics

submitted by

Vincent Mirou Klinkhamer

born in Berkeley, CA, USA

2012

An apparatus for few-fermion systems in multiple well potentials

This Master thesis has been carried out by

Vincent Mirou Klinkhamer

at the

Physikalisches Institut and Max-Planck-Institut für Kernphysik

under the supervision of

Herrn Prof. Dr. Selim Jochim

An apparatus for few-fermion systems in multiple well potentials:

In this thesis, an apparatus which will create few-fermion systems in multiple well potentials is presented. It will be integrated in an existing few-fermion experiment. This experiment can prepare few-fermion systems of up to ten ultracold ^{6}Li atoms deterministically in an optical microtrap. The microtrap consists of the focus of a laser beam (1064 nm wavelength) with a waist of 1.8 μm. In the the course of this thesis a new microtrap setup based on a custom-built, high numerical aperture (NA = 0.55) objective was planned, constructed and tested. With this setup microtraps with sub-micron waists can be created, which will improve the control of the few-fermion systems. Additionally, an acousto-optic deflector (AOD) was characterized and integrated into the setup to allow the creation of multiple well potentials. An interferometric alignment procedure for the setup ensures the quality of the microtraps by minimizing the wavefront errors of the incoming laser beam. This is necessary since a visual diagnosis of the microtraps in the vacuum chamber of the experiment is impossible. In preparation of upcoming experiments, the expected physical parameters of viable microtrap arrays have been calculated numerically.

Ein Apparat für Systeme weniger Fermionen in mehreren Potentialtöpfen:

Diese Arbeit stellt einen Apparat vor, der Systeme mit wenigen Fermionen in Fallenpotentialen bestehend aus mehreren Potentialtöpfen erzeugen soll. Er wird ein bestehendes Experiment erweitern, mit dem Systeme aus bis zu zehn ultrakalten ^{6}Li Atomen in einer optischen Mikrofalle deterministisch präpariert werden können. Diese Mikrofalle besteht aus dem Fokus eines Laserstrahls (1064 nm Wellenlänge) mit einer Strahltaille von 1.8 μm. Im Verlauf dieser Arbeit wurde ein neuer Mikrofallenaufbau mit einem spezialangefertigten Objektiv hoher numerischer Apertur (NA = 0.55) entworfen, gebaut und getestet. Damit ist es möglich, Mikrofallen mit einer Taille von unter einem Mikrometer zu erzeugen, was die Kontrolle der wenig-Fermion Systeme verbessert. Außerdem wurde ein akusto-optischer Deflektor (AOD) charakterisiert und eingebaut, wodurch die Erzeugung von Potentialen mit mehreren Töpfen ermöglicht wird. Ein interferometrisches Verfahren wurde zur Justage des Aufbaus entwickelt. Es gewährleistet die Qualität der Mikrofallen, indem die Wellenfrontfehler des einlaufenden Laserstrahles minimiert werden. Dieses Verfahren ist notwendig, da eine visuelle Überprüfung der Mikrofallen in der Vakuumkammer unmöglich ist. Im Hinblick auf kommende Experimente wurden die zu erwartenden physikalischen Parameter der möglichen Mikrofallenkonfigurationen numerisch berechnet.

Contents

1 Introduction **1**

2 The existing experiment **3**
2.1 Physics of ultracold atoms 3
2.1.1 Scattering and Feshbach resonances - manipulating the interaction potential 3
2.1.2 Optical dipole trapping - manipulating the external potential . 8
2.2 Experimental setup and sequence 8
2.3 The microtrap 11
2.3.1 Creating a few-fermion system 11
2.3.2 The current objective 13

3 Atoms in periodic potentials **15**
3.1 From Bloch states to the single-band Fermi-Hubbard Hamiltonian . . 15
3.2 Predictions of the Hubbard model in the limits $J \gg U$ and $U \gg J$ . . 17
3.3 Solving the full Hubbard model for a double well 19
3.4 Calculating the interaction and tunneling parameters 22

4 The new setup **27**
4.1 Layout of the new setup 27
4.2 The new objective 28
4.2.1 Design 28
4.2.2 Tests 30

5 Radio frequency setup and acousto-optic deflector **35**
5.1 Theory of acousto-optics 35
5.2 Power stabilization of the laser 41
5.3 RF-setup for the AOD 41
5.4 Tests of the AOD 43

6 Conclusion and outlook **49**

A Numerical calculation of the Hubbard parameters in a double well **53**

B Alignment of the optical setup **61**

C Lookup table generation **65**

D Lists **69**
D.1 List of Figures 69
D.2 List of Tables 70

E Bibliography **71**

1 Introduction

Periodic quantum systems play a vital role both for fundamental physics and for the physics of our daily lives. From the models for such systems stem, e.g., the understanding of conducting and insulating materials and the theory of quantum magnetism. Both examples belong to the field of solid state physics which is based on the behavior of quantum (quasi-) particles in the periodic crystal structure of a solid.

Due to the quantum nature of such systems, their complexity increases exponentially with their size [Fey82]. This makes it virtually impossible for theoretical studies to perform exact calculations on conventional computers. Hence one needs to treat periodic quantum systems experimentally. This can be done with real solids, i.e., crystal samples. However, the properties of solids such as the lattice configuration or the interparticle interaction cannot be varied at will making real solids difficult to compare with fundamental theoretical models.

One way of overcoming this problem is to study periodic quantum systems with ultracold atoms in optical lattices. The advances in atom cooling resulted in the creation of an atomic Bose-Einstein condensate (BEC) in the 1990s [Dav95]. This showed that for ultracold atoms, quantum mechanical phenomena can prevail over thermal effects. Once confined in an optical lattice, the ultracold atoms form a periodic quantum system (e.g. [Gre02]). Usually the optical lattices are implemented as standing waves created by overlapping laser beams. The advantage of these systems is their flexibility: the interparticle interaction, the particle density, the lattice depth and the lattice geometry can be varied over a wide range. Thanks to the simplicity of the systems, there are fewer side effects obscuring the phenomena predicted by theoretical models.

One of the challenges for studying quantum systems in optical potentials is the creation of low-entropy systems. Ordering effects as predicted by the Hubbard model cannot be observed if there is too much entropy in the system, e.g. due to thermal effects. For example, the anti-ferromagnetic phase of the Fermi-Hubbard model requires the entropy per particle to be below $s \lessapprox 0.5 \ln 2 \, k_\mathrm{B} \approx 0.35 \, k_\mathrm{B}$ [McK11]. Currently it is not possible to cool the atoms in a lattice to the required temperatures with conventional cooling methods [Jör10].

Our experiment allows us to create low-entropy systems with few particles, albeit in a single microtrap and not in a periodic potential. We prepare our system in such a way that the lowest energy levels are occupied with a high probability. The major part of the entropy of the system is then contained in the higher energetic part which is discarded. The resulting system contains up to ten particles in the ground state, which leads to a vanishing entropy. In order to combine low-entropy

preparation and optical lattices, we are expanding our existing experiment with a setup which generates an optical lattice as an array of microtraps.

This expansion will be the focus of my thesis, as well as the physics and experimental parameters we expect of it. The next chapter will present the theory of ultracold atoms and the operation principle of our existing experiment. Chapter 3 elaborates the theory and predictions of the Hubbard model, as well as the parameter range we will be able to cover. The next two chapters summarize the setup which generates the potential and the testing of its critical components. The last chapter concludes with the measurements we will perform with the new setup and briefly presents modifications which will allow an even wider range of experiments.

2 The existing experiment

2.1 Physics of ultracold atoms

The purpose of experiments with ultracold quantum gases is to study a variety of quantum systems. As it is possible to manipulate the Hamiltonian $H = T + V_{\text{int}} + V_{\text{ext}}$ (where T is the kinetic energy) by, e.g., controlling the interaction potential V_{int} or the external trapping potential V_{ext}, a variety of quantum systems can be realized [Blo08]. This chapter summarizes the theoretical treatment of ultracold atoms and gives an overview of our experiment.

2.1.1 Scattering and Feshbach resonances - manipulating the interaction potential

An interaction between two particles with the same mass m and the coordinates $\boldsymbol{r}_1$ and $\boldsymbol{r}_2$ can be described by the stationary Schrödinger equation

$$H\psi(\boldsymbol{r}_1, \boldsymbol{r}_2) = E\psi(\boldsymbol{r}_1, \boldsymbol{r}_2) \tag{2.1}$$

where $\psi(\boldsymbol{r}_1, \boldsymbol{r}_2)$ is the total wavefunction and the Hamiltonian takes the form

$$H = -\frac{\hbar^2}{2m}\nabla_1^2 - \frac{\hbar^2}{2m}\nabla_2^2 + V_{\text{ext}}(\boldsymbol{r}_1) + V_{\text{ext}}(\boldsymbol{r}_2) + V_{\text{int}}(\boldsymbol{r}_1 - \boldsymbol{r}_2). \tag{2.2}$$

As our interaction has a very short range r_0 (for Van-der-Waals forces it is on the order of 1 Å) compared to the sizes of typical external potentials (on the order of 1 μm), we can assume that the external potential remains constant for interaction processes. We can transform our coordinates into the relative coordinate system with the center of mass coordinate $\boldsymbol{R} = (\boldsymbol{r}_1 + \boldsymbol{r}_2)/2$, the relative coordinate $\boldsymbol{r} = \boldsymbol{r}_1 - \boldsymbol{r}_2$ and the reduced mass $\mu = m/2$. For our problem, we only need to take the relative coordinate into account. Both assumptions allow us to write the stationary Schrödinger equation as

$$\left(-\frac{\hbar^2}{2m}\nabla_{\boldsymbol{r}}^2 + V_{\text{int}}(\boldsymbol{r})\right)\psi_r(\boldsymbol{r}) = E_r\psi_r(\boldsymbol{r}). \tag{2.3}$$

An ansatz for the wavefunction far away from the scattering potential would be that it consists of an incoming plane wave and an outgoing spherical wave

$$\psi_r(\boldsymbol{r}) \propto e^{i\boldsymbol{k}\cdot\boldsymbol{r}} + f(\boldsymbol{k}', \boldsymbol{k})\frac{e^{ikr}}{r}. \tag{2.4}$$

The scattering amplitude f is a function of the momentum of the incoming plane wave and outgoing particle, explicitly

$$f(\boldsymbol{k}', \boldsymbol{k}) = -\frac{\mu}{2\pi\hbar^2} \int d\boldsymbol{r}'\, e^{-i\boldsymbol{k}'\cdot\boldsymbol{r}'} V_{\text{int}}(\boldsymbol{r}')\psi_r(\boldsymbol{r}'). \tag{2.5}$$

If we can find a simple expression for f independently of this equation, we can use it to derive a simple, effective interaction potential.

First, we make use of the symmetry of the problem. We assume that particles with low momenta and consequently large de Broglie wavelengths cannot resolve the details of our interaction potential and we conclude that we therefore can use a spherically symmetric interaction potential $V_{\text{int}}(r)$. The scattered wavefunction will be axially symmetric with respect to the incident wavevector $\boldsymbol{k}$. We can then write our scattered wavefunction with the partial wave expansion (see, e.g., [Mes65])

$$\psi_r(\boldsymbol{r}) = \sum_{l=0}^{\infty} P_l(\cos\theta) R_{k,l}(r) \tag{2.6}$$

using the Legendre polynomials P_l as a function of the angle between the incident and scattered momenta θ. The radial functions can be solved with the radial Schrödinger equation, resulting in

$$R_{k,l}(r) = \frac{u_{k,l}(r)}{r} \propto \frac{1}{r} \sin\left(r - l\frac{\pi}{2} + \delta_l\right). \tag{2.7}$$

If we use this in the previous equation and compare it to the partial wave expansion of equation (2.4), we can identify

$$f(k, \theta) = \frac{1}{2ik} \sum_{l=0}^{\infty} (2l+1)\left(e^{2i\delta_l} - 1\right) P_l(\cos\theta). \tag{2.8}$$

We can also see that each of the components l of the scattered wave only differs by a phase shift δ_l from the components of partial wave expansion of the incident plane wave. So, the effect of a scattering potential on a plane wave is to shift the phase of each of its components separately.

We can further simplify this expression if we take into account that ultracold atoms have very low energies and small wavevectors k. Since the phase shift behaves as $\delta_l \propto k^{2l+1}$ in this regime, we can neglect the terms for $l > 0$, as $(\exp(2i\delta_l) - 1) \approx 0$ when $k \to 0$. Retaining only the so-called s-wave term, the scattering amplitude then looks like

$$f_0 = \frac{1}{2ik}\left(e^{2i\delta_0} - 1\right) = \frac{1}{k\cot\delta_0 - ik}. \tag{2.9}$$

Here we can approximate $k\cot\delta_0 = k/\tan\delta_0 \overset{k \ll 1/r_0}{\approx} -1/a$ with the s-wave scattering length a. The scattering amplitude can now be expressed as

$$f(k) = -\frac{a}{1 + ika} \tag{2.10}$$

and for small values of $k\,|a|$

$$f(k) = -a. \tag{2.11}$$

In this case, the entire physics of the scattering is contained in only one parameter.

Now we can solve our initial equation for the scattering amplitude (2.5)

$$f(\boldsymbol{k}', \boldsymbol{k}) = -\frac{\mu}{2\pi\hbar^2} \int d\boldsymbol{r}'\, e^{-i\boldsymbol{k}'\cdot\boldsymbol{r}'} V_{\text{int}}(\boldsymbol{r}')\psi_r(\boldsymbol{r}')$$

in such a way that it matches our previous result (2.11) in the same limits. We do this in the first Born approximation, where the total wavefunction is $\psi_r(\boldsymbol{r}') = e^{-i\boldsymbol{k}\cdot\boldsymbol{r}'}$, leading to

$$f(\boldsymbol{k}', \boldsymbol{k}) = -\frac{\mu}{2\pi\hbar^2} \int d\boldsymbol{r}'\, e^{-i(\boldsymbol{k}'-\boldsymbol{k})\cdot\boldsymbol{r}'} V_{\text{int}}(\boldsymbol{r}'). \tag{2.12}$$

Here, the scattering amplitude is just the Fourier transform of the potential. The simplest potential to yield a constant scattering amplitude is a delta-interaction potential

$$V_{\text{int}}(\boldsymbol{r}_1, \boldsymbol{r}_2) = g\,\delta(\boldsymbol{r}_1 - \boldsymbol{r}_2), \tag{2.13}$$

if we transform out of the center-of-mass system again. Matching this potential to the scattering amplitude $f = -a$ fixes its coupling strength to

$$g = \frac{4\pi\hbar^2}{m} a. \tag{2.14}$$

If we want to tune our interactions, we have to tune our scattering length $a = -\lim_{k\ll 1/r_0} \tan(\delta_0)/k$. An intuitive way to do this would be varying the depth of our potential g (figure 2.1). For zero potential depth, there is no phase shift between the scattered wavefunction and the incident wavefunction. When one increases the potential depth, the scattered wavefunction in the potential gets an increased oscillation frequency and the part outside has to match it at the edge of the potential. This leads to a positive phase shift and a negative scattering length for small depths. The scattering length can be visualized as the intercept with the abcissa of the linearly extrapolated wavefunction at the edge. When the potential depth is increased, a first bound state appears. The phase shift is now $\pi/2$ and the scattering length diverges $|a| \to \infty$. For even deeper potentials, the phase shift increases further and the scattering length becomes positive.

Directly manipulating the depth of the interaction potential in order to tune a scattering resonance is not possible in the experiment. Instead, we make use of a Feshbach resonance. Our two interacting particles have scattering channels with different energies depending on their internal quantum numbers. For example, the

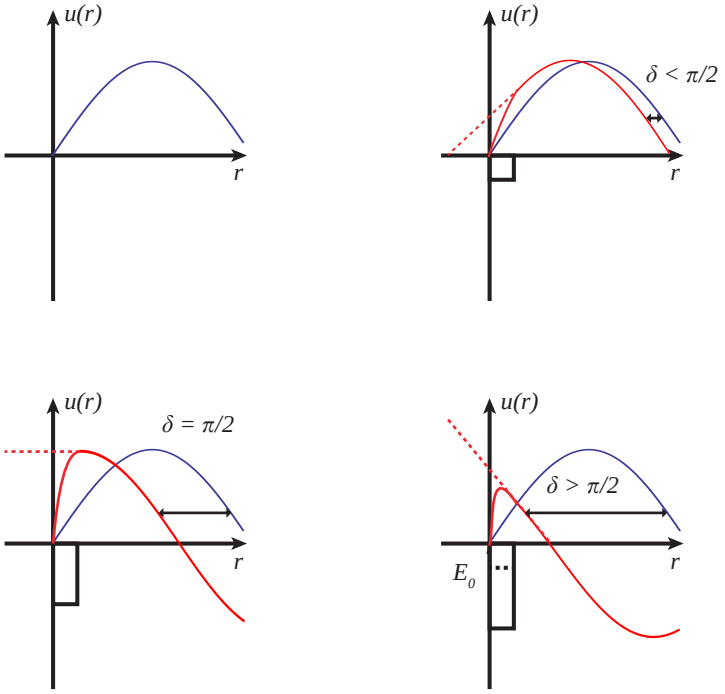

Figure 2.1: Radial wavefunctions $u(r) = r\ R(r)$ for zero potential depth (blue) and for non-zero potential depth (red). The scattered wavefunction acquires a phase shift δ. The scattering length is the intercept of the dashed line with the abcissa. The potential depth of the top left graph is zero. The top right potential contains no bound states. The bottom left (right) potential depth equals (is larger than) the energy of its bound state (black dotted line).

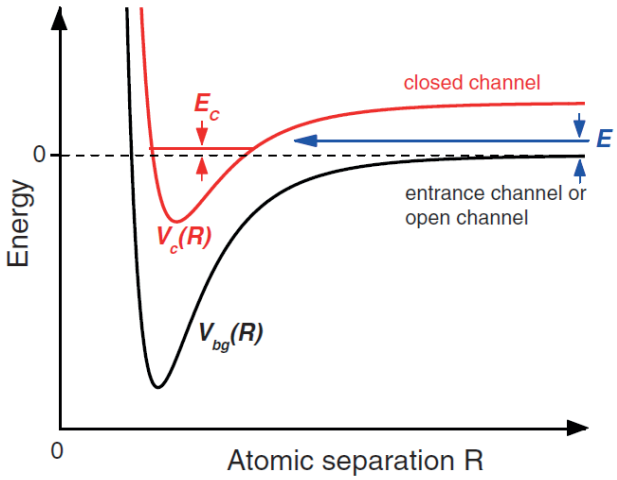

Figure 2.2: Principle of a Feshbach resonance for two particles. The interaction is resonant when the energy E of the incoming particles matches the bound state energy of the closed channel. From [Chi10].

spins can be opposite (singlet configuration) or aligned (triplet configuration). The latter has a higher energy and cannot be reached directly by two incoming particles (hence it is a closed channel). These configurations have different magnetic moments which results in a shift of the relative energy

$$\Delta E = \Delta\mu\, B \tag{2.15}$$

when a magnetic field B is applied. By tuning the magnetic field, ΔE can be tuned and bound states of the closed channel can become resonant with the energy of the incoming particles (figure 2.2). Even though they cannot remain in the closed channel, they can couple to it. Therefore we can manipulate the scattering length using this resonance as a function of B [Chi10]:

$$a = a_{\mathrm{bg}}\left(1 - \frac{\Delta B}{B - B_0}\right) \tag{2.16}$$

where a_{bg} is the background scattering length, B_0 is the magnetic field where the resonance occurs and ΔB is the width of the resonance.

Summarizing, this section shows that the interaction potential of a system consisting of ultracold atoms can be described by a contact interaction $V_{\mathrm{int}}(\boldsymbol{r}_1, \boldsymbol{r}_2) = \frac{4\pi\hbar^2}{m} a\, \delta(\boldsymbol{r}_1 - \boldsymbol{r}_2)$. The strength of the interaction can be controlled with a magnetic offset field via a Feshbach resonance, which allows us to tune the scattering length a.

2.1.2 Optical dipole trapping - manipulating the external potential

An external electric field $\boldsymbol{E}$ will induce an electric dipole moment $\boldsymbol{p} = \alpha\, \boldsymbol{E}$ on a neutral atom. α is the complex polarizability and depends on the frequency of the external electric field. The interaction between the induced dipole moment and the external electric field gives the atom a potential energy

$$U_{dip} = -1/2\, \langle \boldsymbol{p}\, \boldsymbol{E} \rangle \propto -\mathrm{Re}\,(\alpha)\ |E|^2 \tag{2.17}$$

which is proportional to the intensity $I \propto |E|^2$ of the field. Using an approximation of α for the classical oscillator model (which applies for large detunings from the atomic transition) the potential energy takes the form [Gri00]

$$U_{dip} = -\frac{3\pi c^2}{2\omega_0^3} \left(\frac{\gamma}{\omega_0 - \omega} + \frac{\gamma}{\omega_0 + \omega} \right) I(\boldsymbol{r}) \tag{2.18}$$

where c is the speed of light, ω_0 is the frequency of the atomic transition and γ is its spontaneous decay width. If the external field is red detuned ($\omega < \omega_0$), the potential is deepest for maximum intensity.

For a focused Gaussian beam with laser power P propagating in z-direction, the intensity is given as [Sal91]

$$I(r, z) = \frac{2P}{\pi w^2(z)} \exp\left(-2\frac{r^2}{w^2(z)} \right). \tag{2.19}$$

r is the radial coordinate and $w(z) = w_0 \sqrt{1 + \left(\frac{z}{z_R}\right)^2}$ the $1/e^2$-beam radius. The characteristic parameters of the beam are the minimum beam radius w_0 called beam waist and the Rayleigh length $z_R = \pi w_0^2/\lambda$ where the peak intensity has dropped by half compared to the peak intensity in the focal plane.

2.2 Experimental setup and sequence

The atomic species used in the existing experiment is fermionic Lithium ^{6}Li. Its optical transition at 671 nm wavelength can be used for laser cooling. The nuclear spin $I = 1$ and electronic spin $S = 1/2$ couple to $F = I + S$ for weak magnetic fields. In the Paschen-Back regime for magnetic fields above 100 Gauss the energy levels are grouped depending on the magnetic quantum number m_S of the electronic spin as shown in Fig. 2.3. The states $|1\rangle$, $|2\rangle$ and $|3\rangle$ are used in the experiment as they are stable against dipolar relaxation. Atoms in the states $|4\rangle$, $|5\rangle$ and $|6\rangle$ would relax to the energetically lower states of the $m_S = -1/2$ manifold and would be lost from the trap as a consequence. The interactions between the $|1\rangle$, $|2\rangle$ and $|3\rangle$ states are governed by Feshbach resonances. For ^{6}Li the width of the Feshbach resonance is $\Delta B \approx 300$ Gauss which is two orders of magnitude more than for other atoms

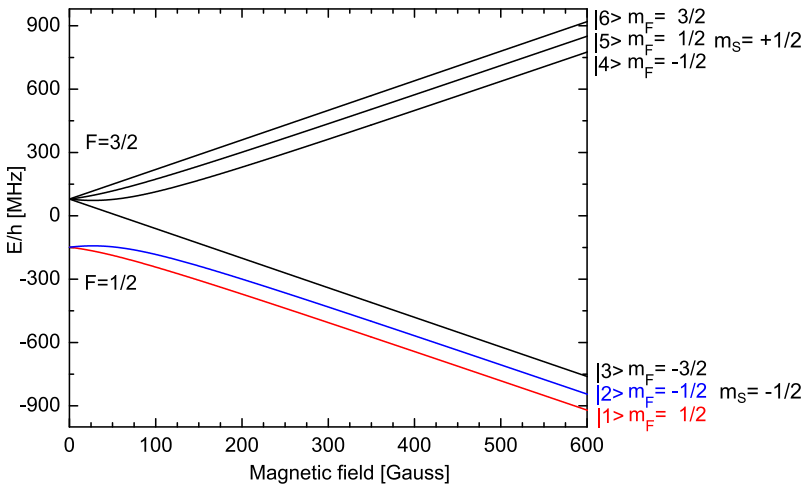

Figure 2.3: Zeeman hyperfine levels of the ground state of ^{6}Li. The magnetic moments can be extracted from the slopes of the curves. From [Ser11a].

[Chi10]. This allows a precise and stable control of the scattering length through the magnetic field.

The vacuum chamber is shown in Fig 2.4. A hot lithium gas is created in the lithium oven. It is slowed down in a Zeeman slower before it reaches the main vacuum chamber (octagon). The Zeeman slower makes use of laser cooling: When an atom absorbs a photon from a laser beam its momentum is changed by $\Delta \boldsymbol{p} = \hbar \boldsymbol{k}$ where $\boldsymbol{k}$ is the wavevector of the photon in direction of the laser beam. The excited atom emits a photon by spontaneous emission. Because this happens isotropically, the average force on the atom is

$$\langle \boldsymbol{F} \rangle = \hbar \boldsymbol{k} \gamma_p. \tag{2.20}$$

The scattering rate

$$\gamma_p = \frac{s_0 \gamma / 2}{1 + s_0 + \left[2\left(\delta + \omega_D\right)/\gamma\right]^2} \tag{2.21}$$

depends on the intensity of the light relative to the saturation intensity $I/I_S = s_0$, the detuning of the laser frequency from the atomic transition $\delta = \omega_L - \omega_A$ and the Doppler shift due to the motion of the atoms $\omega_D = -\boldsymbol{k} \cdot \boldsymbol{v}$ [Met99]. If the laser is tuned to match the initial Doppler shift , the scattering rate will decrease the more the atoms have been decelerated. In order to maintain a high scattering rate (i.e. a high deceleration), the atomic transition frequency ω_A is shifted using the Zeeman effect. The exact specifications of the coils of the Zeeman slower can be found in [Ser07].

The atoms which have been slowed down to below 10 m/s are captured in a magneto-optical trap (MOT). It is composed of counterpropagating laser beams in all three spatial directions which are detuned from the atomic transition frequency

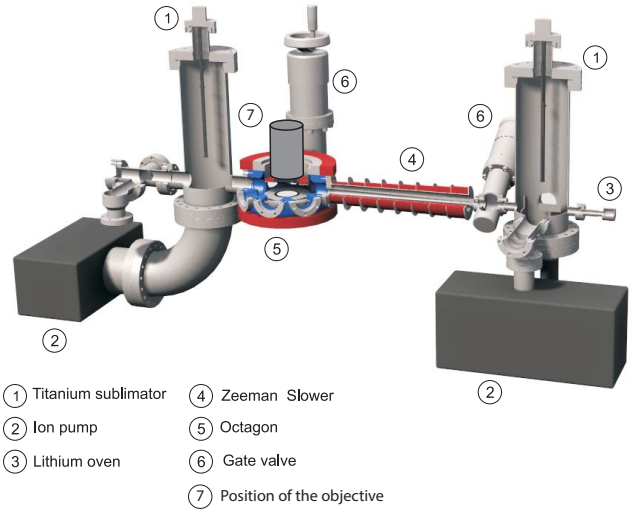

Figure 2.4: Vacuum system. The coils for the Zeeman slower, MOT magnetic field and Feshbach magnetic field are shown in red. From [Ser07].

and a pair of coils in anti-Helmholtz configuration. The detuning of the lasers provides confinement in velocity space and the magnetic field gradient provides confinement in position space (a more detailed explanation can be found in [Met99]). Due to the velocity dependence of the laser force the motion of lithium atoms is damped and they are cooled to approximately 500 μK just above the Doppler temperature $T_D = \frac{\hbar\gamma}{2k_B} = 140\,\mu\text{K}$.

In the next step the atoms are transferred to an optical dipole trap generated by two far red-detuned crossed laser beams ($\lambda = 1070$ nm, waist $w_0 = 40\ \mu$m). The atoms are cooled evaporatively by reducing the depth of the trap, i.e. decreasing the intensity of the laser beams. This cooling scheme requires that the atoms thermalize via collisions during the process. Since there is no interaction between identical fermions, we use a balanced mixture of atoms in the $|1\rangle$ and $|2\rangle$ states. The interaction strength is controlled with a magnetic offset field near the Feshbach resonance. To prevent the formation of bound molecular states, the last part of the evaporation is performed at negative scattering lengths. The final sample consists of about 7.5 10^4 atoms per state at $T/T_F \approx 0.28$. In the next stage, a fraction of these atoms is transferred to a smaller dipole trap — the microtrap. A detailed description of the evaporation process can be found in [Lom11].

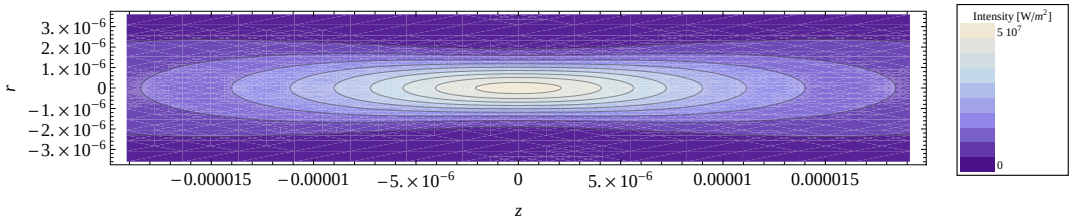

Figure 2.5: Intensity profile of the microtrap in the $z-r$-plane for typical operating parameters (240 μW laser power, waist $w_0 = 1.8\,\mu$m).

2.3 The microtrap

2.3.1 Creating a few-fermion system

A microtrap is a small dipole trap created by a single, strongly focused beam. The radial confinement of the atoms is given by the Gaussian beam profile, similar to the dipole trap of the previous section. The axial confinement is provided by the decrease of the axial intensity at the scale of the Rayleigh range as can been seen from equation (2.19). The intensity profile of a typical microtrap is shown in figure 2.5. Such a microtrap contains approximately 100 energy levels which each can be filled with one particle per spin state if the temperature T of the fermi gas is low enough (high degeneracy). If one now can control the number of energy levels, one controls the number of trapped atoms at the same time.

The starting point of our preparation scheme is to overlap the microtrap and the large dipole trap reservoir without raising the temperature T in the reservoir. Now, the combined Fermi energy is $E_F = E_{\mathrm{F,res}} + E_{\mathrm{F,mt}}$ (res and mt standing for reservoir and microtrap respectively) instead of $E_{F,res}$. One can see from the Fermi distribution of the occupation probability of a state with a low energy E

$$P(E) = \frac{1}{e^{(E-\mu)/k_B T} + 1} \tag{2.22}$$

that for higher E_F this state is more likely to be occupied (fig. 2.6). For low T/T_F, we can assume that $\mu \approx E_F$. For the typical parameters given in figure 2.6 the occupation probability at the lowest energy level $E_0 = \hbar\omega \approx h \cdot 10\,\mathrm{kHz}$ is $P(E_0) > 0.9999$.

Once the large reservoir is turned off, the microtrap contains approximately 100 levels. Each of it is filled with one atom per state with high fidelity. We can acquire the desired number of atoms by spilling atoms out of the microtrap by applying a magnetic field gradient $\nabla \boldsymbol{B}$ for a time t_{spill} along the direction of the microtrap laser beam. This gradient exerts a force $\boldsymbol{F} = \nabla(\boldsymbol{\mu} \cdot \boldsymbol{B})$ on the atoms which leads to a combined axial potential of

$$V(z) = V_0 \left(1 - \frac{1}{1 + (z/z_R)^2}\right) - \mu_B \frac{\partial B}{\partial z} z. \tag{2.23}$$

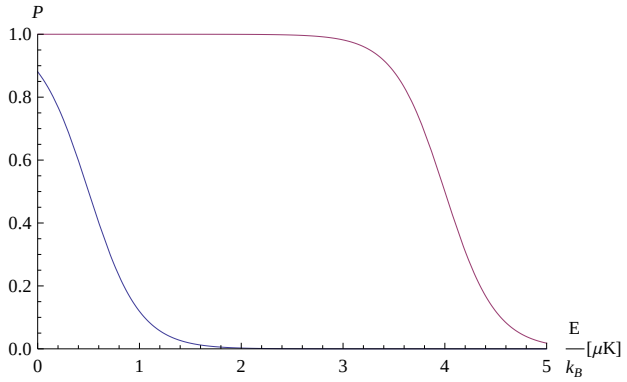

Figure 2.6: Occupation probability $P(E)$ from equation (2.22) with $T_F = T_{F,res} = 0.5\,\mu$K (blue) and $T_F = T_{F,res} + T_{F,mt} = 4\,\mu$K (purple) at $T = 0.25\,\mu$K.

The potential depth V_0 at the center of the trap $(r, z) = 0$ can be calculated from equations (2.18) and (2.19).

To deterministically prepare a system where only the N lowest energy levels are occupied, one has to ensure that the atoms on those levels have a long tunneling time: $\tau_i \gg t_{spill}$, $i = 0 \ldots N-1$. The higher levels have to be emptied with a high probability. This can be achieved if there is no bound state anymore or if the tunneling time $\tau_N \ll t_{spill}$.

The tunneling times τ can be calculated for our potential with the WKB (Wentzel-Kramers-Brillouin) method (explained in detail in, e.g., [Mer98]). The wavefunction for slowly varying potentials should be similar to a linear combination of plane waves and is given by

$$\psi(z) = \sum_{\pm} \frac{C'_{\pm}}{\sqrt{p(z)}}\, e^{\pm i \int^z dz' p(z')/\hbar} \tag{2.24}$$

where $p(z) = \sqrt{2m\,(E - V(z))}$ is the momentum of the atom and $C'_{\pm}$ are coefficients which have to be determined from boundary conditions. Choosing the classical turning points z_1 and z_2 of a bound state as boundary condition, one obtains quantized energy levels E_n which obey

$$\frac{1}{\hbar} \int_{z_1}^{z_2} dz\ \sqrt{2m\,(E_n - V(z))} = \pi\,(n + 1/2)\,. \tag{2.25}$$

Using this formula and the potential along the beam axis $\propto I(0, z)$ from equation (2.23), one can see that a smaller waist w_0 means a larger spacing between the energy levels. Similarly it is possible to calculate the waist and the laser power in the trap by fitting measured energy levels with formula given above.

For $E < V$, p becomes imaginary and the wavefunction decays exponentially. The tunneling transmission probability is

$$|T(E)|^2 = \exp\left(-2 \int_{z_1}^{z_2} dz\ p(z)/\hbar\right). \tag{2.26}$$

The tunneling time depends on the transmission probability and on the rate at which the atom hits the barrier $\nu(E) = E/h$ as

$$\tau(E) = \frac{1}{\nu(E)\ |T(E)|^2}. \tag{2.27}$$

Conversely, a measurement of the tunneling time τ can be used to calculate the magnetic field gradient. The probability to find atoms on a level with energy E_i after a spilling duration t_{spill} is

$$P(E_i) = e^{-t_{spill}/\tau(E_i)}. \tag{2.28}$$

With these methods, we can prepare systems with 2 atoms in the ground state with a fidelity of 96(1)% and systems of 8 atoms in the ground state with 92(2)% fidelity [Ser11b].

2.3.2 The current objective

In order to spill the microtrap with a high level of control, one needs a laser with a stable intensity (as discussed in detail in section 5.2) and a large level spacing in the microtrap, i.e. a small waist. For this purpose, a focusing setup and a special objective are being used (fig 2.7, [Ser11a]). The objective was designed to be as simple as possible: An aspheric lens (Thorlabs AL5040, $f = 40$ mm) creates the focus inside the vacuum chamber. It has a diffraction limited numerical aperture of NA $= 0.35$ at $\lambda = 1064$ nm. To compensate the effects of the 6 mm thick vacuum viewport, a positive meniscus lens ($f = 800$ mm) was added, increasing the NA to 0.44. As the beam used in the experiment has a diameter of $d = 30$ mm, the NA is reduced to 0.37. The theoretical, diffraction limited waist of this setup is

$$w_0^{theo} = K\frac{\lambda}{2\ \mathrm{NA}} = 1.3\,\mu\mathrm{m}. \tag{2.29}$$

Here, $K \approx 0.87$ is a numerical factor which takes the truncation of the Gaussian beam into account [CVI09]. The aspect ratio of a trap in the harmonic approximation is [Gri00]

$$\eta = \frac{\omega_\perp}{\omega_\parallel} = \frac{\sqrt{\frac{4V_0}{mw_0^2}}}{\sqrt{\frac{2V_0}{mz_R^2}}} = \sqrt{2}\pi\frac{w_0}{\lambda}, \tag{2.30}$$

which for our parameters gives $\eta \approx 10$.

The performance of the objective has been tested in two different ways. The waist of the focus was measured as $w_x = (1.2 \pm 0.1)\ \mu$m and $w_y = (1.3 \pm 0.1)\ \mu$m by imaging the focus with a second, identical objective. The resolution was measured as $r_x = r_y = (1.6 \pm 0.1)\ \mu$m by imaging a $0.8\,\mu$m pinhole with the objective. The waist has also been calculated by fitting the WKB-fomula (2.25) to the experimentally measured energy levels of the microtrap. This resulted in $w_0 \approx 1.8 \pm 0.1\ \mu$m.

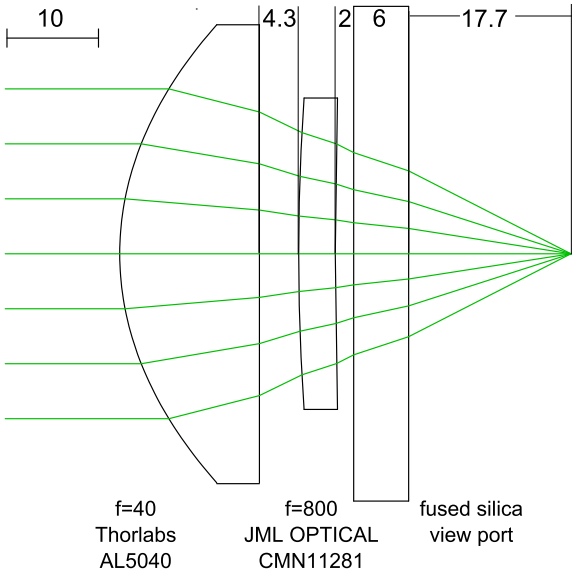

Figure 2.7: The two lenses of the objective (left) and the viewport of the vacuum chamber. Units in mm. From [Ser11a]

3 Atoms in periodic potentials

Quantum systems in periodic potential play a crucial role in solid state physics. Exact solutions are often not possible due to the sheer size of those systems, but with some approximations, the Hubbard model is well suited to describe these systems [Hub63]. Using the techniques from chapter 2, we will be able to produce few fermion systems in periodic potentials with low energy and low entropy, conditions required for the Hubbard model to apply. In this chapter, we will examine whether we can reach the interesting regimes with our setup. The basic explanation of the Hubbard model will follow the lines of [Dua05], [Sca07] and [Tro08].

3.1 From Bloch states to the single-band Fermi-Hubbard Hamiltonian

The Hamiltonian of our system is

$$H = T + V + V_{\text{int}} \tag{3.1}$$

where $T = \frac{p^2}{2m} = -\frac{\hbar^2\nabla^2}{2m}$ is the kinetic energy term, V is the external potential[1] and V_{int} describes the inter-particle interaction. One of the first studies on Fermions in periodic potentials without interaction ($V_{\text{int}} = 0$) was performed by F. Bloch [Blo29]. A periodic potential is invariant for translations by a lattice vector $\boldsymbol{R}$, i.e., $V(\boldsymbol{r} + \boldsymbol{R}) = V(\boldsymbol{r})$. The eigenstates of the Hamiltonian (also called Bloch states) can be expressed by a product of plane waves and a periodic function

$$\psi_{n\boldsymbol{k}}(\boldsymbol{r}) = e^{i\boldsymbol{k}\cdot\boldsymbol{r}} u_{n\boldsymbol{k}}(\boldsymbol{r}) \tag{3.2}$$

where $u_{n\boldsymbol{k}}(\boldsymbol{r}) = u_{n\boldsymbol{k}}(\boldsymbol{r} + \boldsymbol{R})$ with the principle quantum number n and the wave vector $\boldsymbol{k}$. As we want to study the properties of systems with multiple fermions, it is convenient to work with Fock states. They are generated by the creation (annihilation) operators $a^\dagger_{n\boldsymbol{k}\sigma}$ ($a_{n\boldsymbol{k}\sigma}$) which create (annihilate) a fermion in the state $|n, \boldsymbol{k}, \sigma\rangle$. These operators obey the anticommutation relations

[1] Our external potential will not contain an explicit overall trapping potential as in, e.g., [Sch08]. This is already provided by our microtraps themselves.

$$\left\{a^\dagger_{n\boldsymbol{k}\sigma}, a_{n'\boldsymbol{k}'\sigma'}\right\} = \delta_{nn'}\delta_{\boldsymbol{k}\boldsymbol{k}'}\delta_{\sigma\sigma'} \tag{3.3a}$$

$$\left\{a_{n\boldsymbol{k}\sigma}, a_{n'\boldsymbol{k}'\sigma'}\right\} = 0 \tag{3.3b}$$

$$\left\{a^\dagger_{n\boldsymbol{k}\sigma}, a^\dagger_{n'\boldsymbol{k}'\sigma'}\right\} = 0. \tag{3.3c}$$

The Bloch states are non-localized and form a set of basis functions for the Hamiltonian with a periodic potential. By a Fourier transform of the basis, one obtains localized Wannier functions [Wan37]

$$w_n(\boldsymbol{r} - \boldsymbol{R}_j) = \frac{1}{\sqrt{N}} \sum_{\boldsymbol{k}} e^{i\boldsymbol{k}\cdot\boldsymbol{R}_j} \psi_{n\boldsymbol{k}}(\boldsymbol{r}) \tag{3.4}$$

centered on the lattice site $\boldsymbol{R}_j$ where N is the number of lattice sites. The corresponding creation (annihilation) operators are $a^\dagger_{jn\sigma} = \frac{1}{\sqrt{N}} \sum_k e^{i\boldsymbol{k}\cdot\boldsymbol{R}_j} a^\dagger_{n\boldsymbol{k}\sigma}$ ($a_{jn\sigma} = \frac{1}{\sqrt{N}} \sum_k e^{i\boldsymbol{k}\cdot\boldsymbol{R}_j} a_{n\boldsymbol{k}\sigma}$) and satisfy anticommutation relations equivalent to equations (3.3).

Now we can define our fermionic field operators as

$$\Psi^{(\dagger)}_\sigma(\boldsymbol{r}) = \sum_{j,n} a^{(\dagger)}_{jn\sigma} w_n(\boldsymbol{r} - \boldsymbol{R}_j). \tag{3.5}$$

Inserting them into our Hamiltonian gives us

$$H = \sum_\sigma \int d\boldsymbol{r}\; \Psi^\dagger_\sigma(\boldsymbol{r})\,(T+V)\,\Psi_\sigma(\boldsymbol{r}) + \iint d\boldsymbol{r} d\boldsymbol{r}'\; V_{\text{int}} \Psi^\dagger_\downarrow(\boldsymbol{r}')\Psi^\dagger_\uparrow(\boldsymbol{r}')\Psi_\downarrow(\boldsymbol{r})\Psi_\uparrow(\boldsymbol{r}). \tag{3.6}$$

Taking into account only one energy level (i.e. dropping n), nearest neighbor hopping (denoted in the first sum by $\langle i,j\rangle$) and on-site interaction, we get

$$H = -\sum_{\sigma,\langle i,j\rangle} J\; a^\dagger_{i\sigma} a_{j\sigma} + \sum_j U\; a^\dagger_{j\downarrow} a_{j\downarrow} a^\dagger_{j\uparrow} a_{j\uparrow} \tag{3.7}$$

where the hopping and on-site interaction parameters are defined as

$$J = \int d\boldsymbol{r}\; w(\boldsymbol{r} - \boldsymbol{R}_i)\,(T+V)\,w(\boldsymbol{r} - \boldsymbol{R}_j) \text{ and} \tag{3.8}$$

$$U = V_{\text{int}} \int d\boldsymbol{r}\; w(\boldsymbol{r} - \boldsymbol{R}_j) w(\boldsymbol{r} - \boldsymbol{R}_j) w(\boldsymbol{r} - \boldsymbol{R}_j) w(\boldsymbol{r} - \boldsymbol{R}_j). \tag{3.9}$$

As explained in section 2.1.1, the interaction potential is given by $V_{\text{int}} = \frac{4\pi\hbar^2 a}{m a_T^3}$ $\delta(\boldsymbol{r}_1 - \boldsymbol{r}_2)$ with the scattering length $a = a_{\text{bg}}\left(1 - \frac{\Delta B}{B - B_0}\right)$. It has been rescaled by

the trap size $a_T = \sqrt{\frac{\hbar}{m\omega_T}}$ [Kes09] with the trapping frequency ω_T. If we introduce a chemical potential μ and the number operator $n_{j\sigma} = a^\dagger_{j\sigma} a_{j\sigma}$, the single-band Hubbard Hamiltonian reads

$$H = -J \sum_{\sigma,\langle i,j\rangle} a^\dagger_{i\sigma} a_{j\sigma} + U \sum_j n_{j\downarrow} n_{j\uparrow} - \mu \sum_j \left(n_{j\downarrow} + n_{j\uparrow}\right). \tag{3.10}$$

The kinetic term contains the tunneling parameter J and describes the hopping of the atoms between neighboring sites. The interaction term accounts for the interaction energy U between the atoms when they are on the same site. The last term expresses the energy related to the total number of atoms in the system.

The notation of this Hamiltonian shows one great advantage of the Hubbard model: It does not require the exact knowledge of the wavefunctions. The Wannier functions do enter in the parameters J and U, but these parameters can be treated as numbers when calculating observables such as the mean atom number per site. We can intuitively understand our systems in terms of discrete particles on distinct sites. First we will look at two limiting cases before calculating the full Hamiltonian for a double well. The explicit calculation of the Hubbard parameters is shown in the last section of this chapter.

3.2 Predictions of the Hubbard model in the limits $J \gg U$ and $U \gg J$

One limiting case of the Hubbard model is when tunneling is allowed but there is no interaction ($U = 0, J \neq 0$). It is more convenient to describe the operators in momentum space ($a^{(\dagger)}_{\boldsymbol{k}\sigma}$). When applying periodic boundary conditions, our Hamiltonian becomes

$$H = \sum_{\boldsymbol{k},\sigma} \left(\epsilon_{\boldsymbol{k}} - \mu\right) a^\dagger_{\boldsymbol{k}\sigma} a_{\boldsymbol{k}\sigma} \tag{3.11}$$

with the prefactor $\epsilon_{\boldsymbol{k}} = -2J \sum_d \cos(k_d)$ for the case of a square lattice in d dimensions. As expected $\epsilon_{\boldsymbol{k}}$ is the dispersion relation with a bandwidth of $4J$. In this limit, a superfluid phase is formed.

In the other limit tunneling is suppressed ($J = 0$) which gives us the Hubbard physics of a single site. The Hamiltonian reduces to $H = U \sum_j n_{j\downarrow} n_{j\uparrow} - \mu \sum_j \left(n_{j\downarrow} + n_{j\uparrow}\right)$ and we can calculate the partition function

$$Z = \sum_\alpha \langle\alpha| e^{-\beta H} |\alpha\rangle = 1 + 2e^{\beta\mu} + e^{2\beta\mu - \beta U}. \tag{3.12}$$

by summing over all states $|\alpha\rangle$. Now we can calculate quantities such as the mean energy E or the mean occupation ρ:

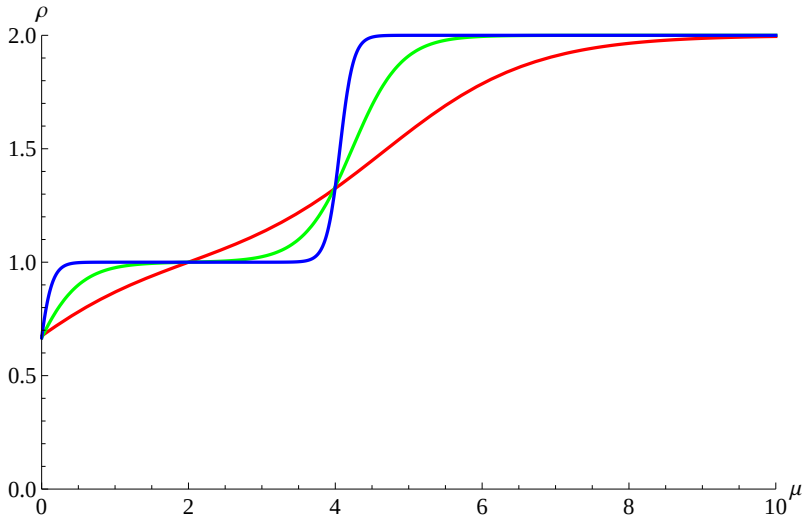

Figure 3.1: Occupation ρ vs. chemical potential μ with $U = 4$ for temperatures $T = 1, 3, 11$ (blue, green, red) in natural units.

$$E = \langle H + \mu n \rangle = Z^{-1} \sum_{\alpha} \left\langle \alpha \left| (H + \mu n)\, e^{-\beta H} \right| \alpha \right\rangle = \frac{U e^{2\beta\mu - \beta U}}{1 + 2e^{\beta\mu} + e^{2\beta\mu - \beta U}} \tag{3.13}$$

$$\rho = \langle n \rangle = \frac{2\left(e^{\beta\mu} + e^{2\beta\mu - \beta U}\right)}{1 + 2e^{\beta\mu} + e^{2\beta\mu - \beta U}}. \tag{3.14}$$

For repulsive interactions $U > 0$, the occupation clearly shows signs of a Mott insulating state for low temperatures (figure 3.1): Only when μ is larger than the energy gap of the size U the occupation jumps to two. For even larger chemical potentials, the occupation does not increase, indicating a band insulator. These and other phenomena (e.g., effects concerning magnetism) can also be described by the local moment

$$\left\langle m^2 \right\rangle = \left\langle (n_\uparrow - n_\downarrow)^2 \right\rangle \tag{3.15}$$

which is one for a singly occupied site and zero else. For strong interaction, all sites are singly occupied and the moment over the entire sample is one. For high temperatures, singly occupied sites are as likely as sites with an even occupation number, so the average moment is 1/2. The number of doubly occupied sites is

$$d = \langle n_\uparrow n_\downarrow \rangle = \frac{1}{2}\left(\langle n_\uparrow + n_\downarrow \rangle - \left\langle m^2 \right\rangle \right). \tag{3.16}$$

Using this observable, the Mott insulating state of an ultracold Fermi gas has been observed experimentally in an optical lattice [Sch08; Jör08].

Dim.	States	Hamiltonian
1	$\|\cdot,\cdot\rangle$	0
1	$\|\uparrow,\uparrow\rangle$, $\|\downarrow,\downarrow\rangle$	0
1	$\|\uparrow\downarrow,\uparrow\downarrow\rangle$	2U
2	$\|\cdot,\uparrow\rangle$, $\|\uparrow,\cdot\rangle$, $\|\cdot,\downarrow\rangle$, $\|\downarrow,\cdot\rangle$	$\begin{pmatrix} 0 & -J \\ -J & 0 \end{pmatrix}$
2	$\|\uparrow\downarrow,\uparrow\rangle$, $\|\uparrow,\uparrow\downarrow\rangle$, $\|\uparrow\downarrow,\downarrow\rangle$, $\|\downarrow,\uparrow\downarrow\rangle$	$\begin{pmatrix} U & -J \\ -J & U \end{pmatrix}$
4	$\|\uparrow,\downarrow\rangle$, $\|\downarrow,\uparrow\rangle$, $\|\uparrow\downarrow,\cdot\rangle$, $\|\cdot,\uparrow\downarrow\rangle$	$\begin{pmatrix} 0 & 0 & -J & -J \\ 0 & 0 & J & J \\ -J & J & U & 0 \\ -J & J & 0 & U \end{pmatrix}$

Table 3.1: Dimensionality, states and Hamiltonians of the subspaces of the 2-site Hubbard model.

3.3 Solving the full Hubbard model for a double well

Now we want to treat the full Hamiltonian (3.10) for non-zero J and U while keeping the particle number fixed ($\mu = 0$). In the previous section, the Hamiltonians of the limiting cases could be diagonalized easily for arbitrarily large lattices. This is not the case anymore for the full Hamiltonian, since the kinetic term scales with $a^{(\dagger)2}$ and the interaction term with $a^{(\dagger)4}$. However, for finite lattice sizes, one can still find exact solutions by the exact diagonaliziation method.

This method is particularly interesting for us in the case of a double well because it is the simplest multi-well potential achievable with the new setup. The problem is described by a 16-dimensional Hilbert space as there are 16 possible states (each site can have no atoms, $\uparrow$, $\downarrow$ or $\uparrow\downarrow$). The Hamiltonian has a block-diagonal form with four 1-dimensional, four 2-dimensional and one 4-dimensional subspace. The corresponding states and Hamiltonians can be found in table 3.1.

In the case of zero particles, four particles or two particles with the same spin, there are no dynamics and the eigenenergies and eigenstates are trivial. If there is one particle in the double well, it may sit on one or the other site. Its eigenstate is a superposition thereof and its eigenenergy depends on the tunneling parameter J. The expectation value of the energy is $\langle E\rangle = -J\tanh(\beta J)$, it decreases with increasing J because the particle can minimize its kinetic energy if it is allowed to delocalize across multiple lattice sites. Three particles in a double well behave analogously to the one-particle case, but the energy of the system is shifted by the interaction energy U.

If there are two particles of different spins in the double well, the system has four eigenstates:

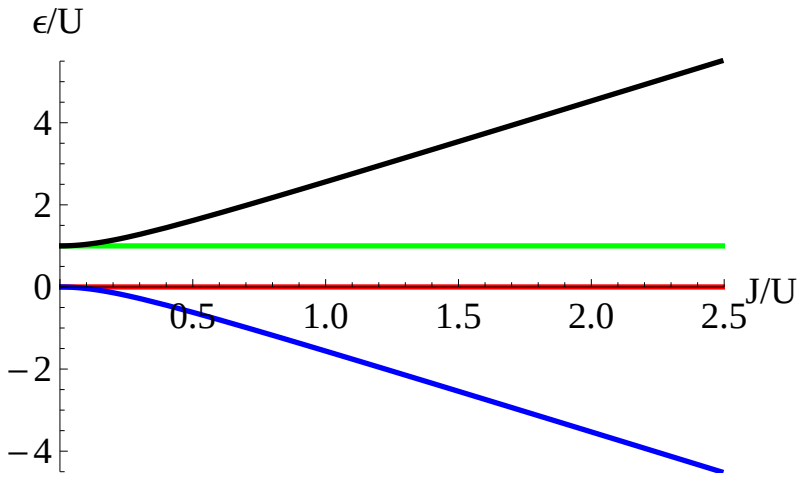

Figure 3.2: Eigenenergies of one spin ↑ and one ↓ particle in a double well for $U = 1$ depending on J. ϵ_+ is black, ϵ_- blue, ϵ_3 red and ϵ_4 green.

$$|\psi_\pm\rangle = \frac{\left(|\uparrow,\downarrow\rangle - |\downarrow,\uparrow\rangle - \frac{\epsilon_\pm}{2J}\left(|\uparrow\downarrow,\cdot\rangle + |\cdot,\uparrow\downarrow\rangle\right)\right)}{\sqrt{2 + 2\epsilon_\pm^2/(2J)^2}} \tag{3.17a}$$

$$|\psi_3\rangle = \frac{1}{\sqrt{2}}\left(|\uparrow,\downarrow\rangle + |\downarrow,\uparrow\rangle\right) \tag{3.17b}$$

$$|\psi_4\rangle = \frac{1}{\sqrt{2}}\left(|\uparrow\downarrow,\cdot\rangle - |\cdot,\uparrow\downarrow\rangle\right). \tag{3.17c}$$

The respective eigenenergies

$$\epsilon_\pm = \frac{U}{2}\left(1 \pm \sqrt{\left(\frac{4J}{U}\right)^2 + 1}\right) \tag{3.18a}$$

$$\epsilon_3 = 0 \tag{3.18b}$$

$$\epsilon_4 = U \tag{3.18c}$$

are shown in figure 3.2. If we look at strong interactions $U \gg J$, the lowest eigenenergy is $\epsilon_- \approx -4J^2/U$. Its eigenstate $|\psi_-\rangle \approx \frac{\left(|\uparrow,\downarrow\rangle - |\downarrow,\uparrow\rangle - \frac{2}{U}\left(|\uparrow\downarrow,\cdot\rangle + |\cdot,\uparrow\downarrow\rangle\right)\right)}{\sqrt{2+8/U^2}} \approx \frac{1}{\sqrt{2}}\left(|\uparrow,\downarrow\rangle - |\downarrow,\uparrow\rangle\right)$ indicates that the ground state of the Hubbard model at half filling is a singly occupied, anti-ferromagnetic configuration.

Now we can study how the method of preparation affects the state in the trap. Herefore we keep β and U fixed. If we prepare a double well with both particles on one site and the other one empty, our initial state is $|\psi(0)\rangle = |\uparrow\downarrow,\cdot\rangle$. Suppose that at the beginning, the barrier between the wells is infinitely high, then we can describe this state as a single well problem with the energy U ($J = 0$). If we

suddenly (diabatically) decrease the barrier to $J \approx U$, our state will evolve into a superposition of $|\psi_+\rangle$, $|\psi_-\rangle$ and $|\psi_4\rangle$ states. If we increase J adiabatically, our state will evolve into the $|\psi_4\rangle$ state for reasons of energy conservation (figure 3.2). One problem emerges, however, if J becomes very large: then it is not possible anymore to speak of wavefunctions localized on lattice sited which was used in the derivation of the Hubbard model and off-site interactions can be of the same order as the on-site interactions [Sca05].

In order to take this into account, we have to reconsider the full Hamiltonian (3.6). Hitherto, we only used the parts proportional to $w^4(\boldsymbol{r} - \boldsymbol{R}_j)$ of the second term. This means that only the wavefunction overlap on the same site is taken into account. Now, we also allow interparticle interactions when the particles are on neighboring sites. The resulting additional terms for Hamiltonian (3.7) read

$$U_{NN} \sum_{\langle i,j \rangle} \left(n_{i\uparrow} n_{j\downarrow} - a^\dagger_{i\uparrow} a^\dagger_{j\downarrow} a_{i\downarrow} a_{j\uparrow} - a^\dagger_{i\uparrow} a^\dagger_{i\downarrow} a_{j\downarrow} a_{j\uparrow} \right) \text{ and} \tag{3.19}$$

$$\Delta J \sum_{\langle i,j \rangle, \sigma \neq \sigma'} n_{i\sigma} \left(a^\dagger_{i\sigma'} a_{j\sigma'} + a^\dagger_{j\sigma'} a_{i\sigma'} \right). \tag{3.20}$$

The first term describes the off-site interaction and is proportional to the density overlap on one site for particles which are centered on neighboring sites: $U_{NN} = V_{\text{int}} \int d\boldsymbol{r}\, w^2(\boldsymbol{r} - \boldsymbol{R}_i) w^2(\boldsymbol{r} - \boldsymbol{R}_j)$. The second term modifies the tunneling depending on the on-site density to $J' = J - \Delta J$ where $\Delta J = V_{\text{int}} \int d\boldsymbol{r}\, w^3(\boldsymbol{r} - \boldsymbol{R}_i) w(\boldsymbol{r} - \boldsymbol{R}_j)$. In the limit for two completely separated sites ($J = 0$), the wavefunctions of the different sites do not overlap and both aforementioned parameters are zero. For the case of two completely overlapping sites ($\boldsymbol{R}_i = \boldsymbol{R}_j$), the wavefunctions of the "different" sites completely overlap and $U_{NN} = \Delta J = U$. As ΔJ goes linearly and U_{NN} quadratically with the off-site overlap, ΔJ is always larger than U_{NN}. Written in matrix notation, this extended Hubbard model (EHM) introduces new off-diagonal terms to the Hamiltonian for the $|\psi_\pm\rangle$ states. The new eigenenergies

$$\begin{aligned} \epsilon_\pm &= \frac{U - U_{NN}}{2} \left(1 \pm \sqrt{\left(\frac{4J'}{U - U_{NN}} \right)^2 + 1} \right) + 2U_{NN} \\ \epsilon_3 &= 0 \\ \epsilon_4 &= U - U_{NN} \end{aligned} \tag{3.21}$$

are shown in figure 3.3. The eigenenergy ϵ_4 drops to zero as tunneling is more and more allowed because the fermions try to minimize their overlap due to the repulsive interaction.

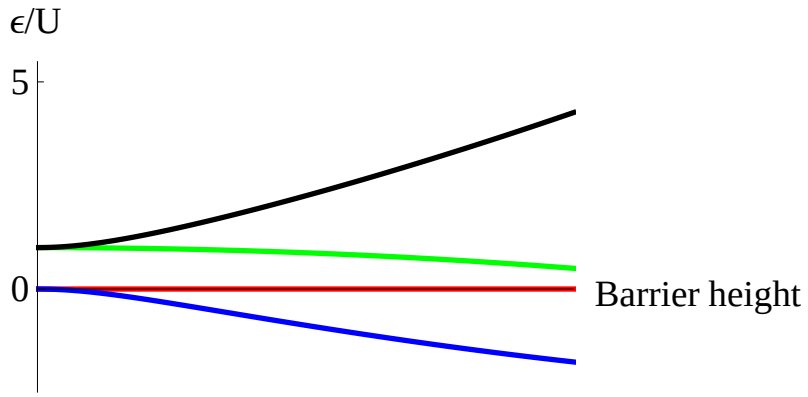

Figure 3.3: Eigenenergies of the Hubbard model with off-site interaction in dependence of the barrier height between the sites. The barrier height decreases from left to right, which is equivalent to an increase of J. Note that this is not an exact solution as U_{NN} and ΔJ have only been approximated to their asymptotic behavior. ϵ_+ is black, ϵ_- blue, ϵ_3 red and ϵ_4 green.

3.4 Calculating the interaction and tunneling parameters

In the previous section, we have found solutions to the Fermi-Hubbard Hamiltonian while treating the Hubbard parameters as numbers. However, in order to compare an experiment with the theoretical Hubbard model, we have to calculate those numbers explicitly. Therefore we have to know the wavefunctions in the potential.

The first step is calculating our potential. It is formed by two microtraps as described in section 2.1.2. We will restrict ourselves to the axis connecting the two wells, making it a 1D problem. Along this axis, the intensity profile of the single beams is Gaussian. We assume that both beams have the same intensity, so the total intensity profile is given by

$$I(x,d) = I_0 \left(e^{-\frac{(x-d)^2}{2\sigma^2}} + e^{-\frac{(x+d)^2}{2\sigma^2}} \right) \tag{3.22}$$

where $2d$ is the distance between the centers of the beams and 2σ is the $1/e^2$ beam waist. The characteristics of this potential strongly depend on the separation of the beams. For large separations ($d > \sigma$), there is an intensity minimum between two maxima, for smaller separations, there is only one maximum (figure 3.4a). The position of the extrema is determined by the transcendental equation $x/\sigma = d/\sigma \tanh(dx/\sigma^2)$ (figure 3.4b). An important quantity of this potential is the trapping frequency, which can be calculated with $U_{dip}(d)$ from equation (2.18) as $\omega_T = \sqrt{k/m} = \sqrt{-U_{dip}(d)/(m\sigma^2)}$ in the harmonic approximation of one of the intensity maxima.

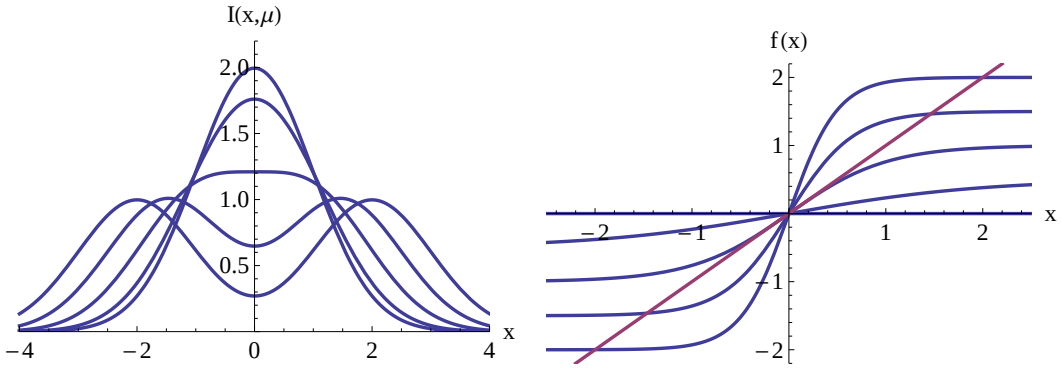

(a) (b)

Figure 3.4: (a) Intensity profiles (eq. (3.22)) and (b) position of the extrema for $x/\sigma = d/\sigma \tanh(dx/\sigma^2)$ for $\sigma = 1$ and $d = 0, 0.5, 1.0, 1.5, 2.0$.

With the potential, we calculate the single-particle 1D wavefunction numerically using a script adapted from [Eve10] by solving the Schrödinger equation with a discretized coordinate $x \to x_i,\ \Psi(x_i) \to \Psi_i,\ x_{i+1} - x_i = \Delta x$:

$$H\Psi_i = -\frac{\hbar^2}{2m}\frac{(\Psi_{i+1} - \Psi_i)/\Delta x - (\Psi_i - \Psi_{i-1})/\Delta x}{\Delta x} + V\Psi_i = E_i\Psi_i. \tag{3.23}$$

After finding the eigenenergies and eigenvectors, one can bring the wavefunctions of the lowest-lying symmetric and antisymmetric states into the left-right (LR) basis according to $\Psi_{L/R} = (\Psi_S \pm \Psi_A)/\sqrt{2}$. Suppose one starts with an atom in the left site, i.e. $\Psi(t = 0) = \Psi_L$, then the tunneling is described by

$$T = \left| \int dx\ \Psi^*(t)\Psi_L \right|^2 = \cos^2\left(\frac{E_S - E_A}{2\hbar}t\right). \tag{3.24}$$

The tunneling parameter J can be calculated as

$$\begin{aligned} J &= \langle\Psi_R| H |\Psi_L\rangle \\ &= \frac{1}{2}\left(\langle\Psi_S| - \langle\Psi_A|\right) H \left(|\Psi_S\rangle + |\Psi_A\rangle\right) \\ &= \frac{E_S - E_A}{2} \end{aligned} \tag{3.25}$$

and the parameters U, ΔJ and U_{NN} can be obtained by using the L/R-wavefunctions as the Wannier functions for the numerical integration. In figures 3.5 and 3.6, some exemplary wavefunctions and parameters are shown. Note that the parameters have been converted to trapping frequencies by division by Planck's constant h for easier comparison with the values from the existing experiment. Figure 3.6e shows that even for a fixed separation, the ratio J/U can be varied by over five orders of magnitude by tuning the laser power between 0.1 and 2.0 mW. From figure 3.6f one

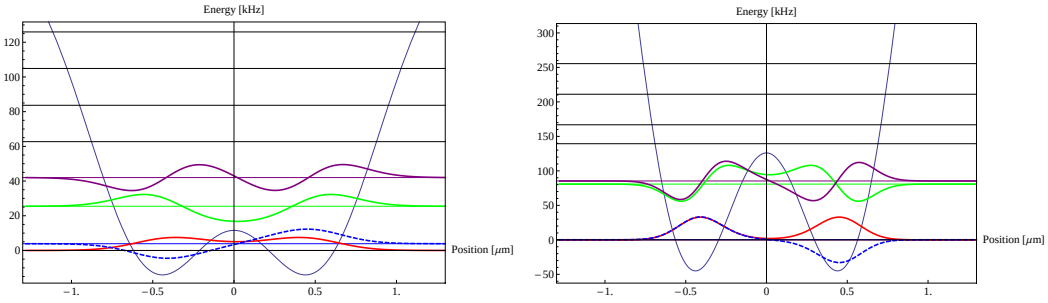

(a) (b)

Figure 3.5: Potentials, energy levels and wavefunctions for a double well created by focused laser beams with a waist of $w_0 = 0.8\,\mu$m, a separation of $2d = 1.0\,\mu$m and a laser power of 0.15 mW (a) and 1 mW (b) each. The first four energy levels and wavefunctions are shown in red, blue, green and purple respectively.

can see that for tunneling parameters $J \gtrapprox 1000$, the parameters ΔJ and U_{NN} (which drops much faster than ΔJ) can be neglected. Keep in mind that the parameters in the real experiment will not exactly match the calculated parameters, as the calculation was performed only in 1D.

The complete code for the numerics can be found in appendix A.

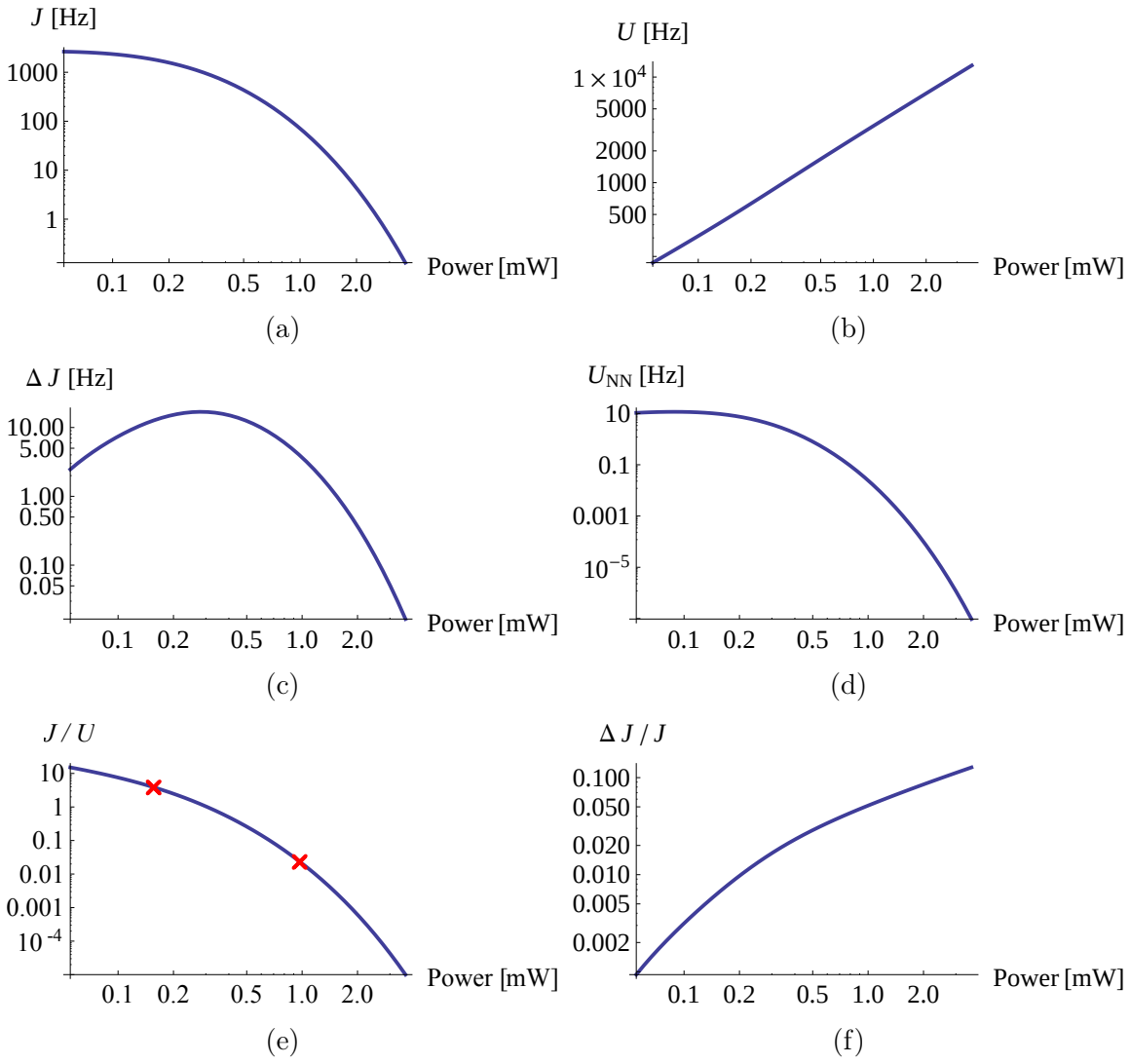

Figure 3.6: Numerical results for the parameters of the Hubbard model. The separation was kept constant at 1 μm, the scattering length was set to $a = 100$ Bohr radii and the laser power was varied between $5\ 10^{-2}$ mW and 4 mW. The red crosses indicate the settings from figure 3.5.

4 The new setup

The new setup has several goals: Its primary purpose is to create a flexible array of microtraps which is realized by adding an acousto-optic deflector (AOD) to the setup. It creates multiple beams which enter the objective at different angles and thus form foci at different postitions after the objective. The properties of the AOD are described in the next chapter. In addition, a new objective designed in [Ser11a] has been assembled by Jenoptik. The layout of the new optical setup is explained in the first part of this chapter. The design and testing of the new objective is discussed in the second part.

4.1 Layout of the new setup

The addition of an AOD and a new objective to the apparatus creating the microtrap requires extensive modifications of the setup. As the planning and constructing of those modifications were projected to take several months, it was decided to build and test an entirely new setup on a breadboard seperate from the main experiment. Other than the organizational advantages, this also allows tests which could not have been performed otherwise, such as the direct observation of the focus of the new objective. After the testing the new setup will replace the current setup at the main experiment.

A schematic of the new setup is shown in fig. 4.1. A 1064 nm laser beam with a $1/e^2$-diameter of (1.23 ± 0.02) mm is coupled out of a single mode fiber. Its polarization is cleaned by a $\lambda/2$-waveplate and a polarizing beam splitter (PBS). The waveplate after the PBS is used for diagnostics when a laser beam is sent in the reverse direction. The beam is then reflected into the AOD which is mounted on a modified 2-axis kinematic mirror mount. The mount is enables us to optimize the diffraction efficiency in both transverse directions by tuning the angle of the AOD and mirror in front of it. After the AOD, the 0^{th} order beam and its higher orders enter a fiber coupler. The fiber coupler consists of an aspheric lens (focal length $f = 18.56$ mm, Thorlabs C280TME-B) and a FC/APC fiber adapter. The fiber adaper is mounted in a XY-mount, so it can be displaced relative to the lens in directions transversal to the beam. It now fulfills two roles: When it is coaxial with the lens, a fiber can be mounted for diagnostics with a beam in the reverse direction. When the fiber adapter is displaced from the beam axis, it can be used to block undesired orders produced by the AOD since the fiber adapter is exactly in the focal plane of the aspheric lens.

The $f = 18$ mm lens forms a telescope together with a $f = 300$ mm plano-convex lens which increases the beam diameter to approximately 19.9 mm. The first and

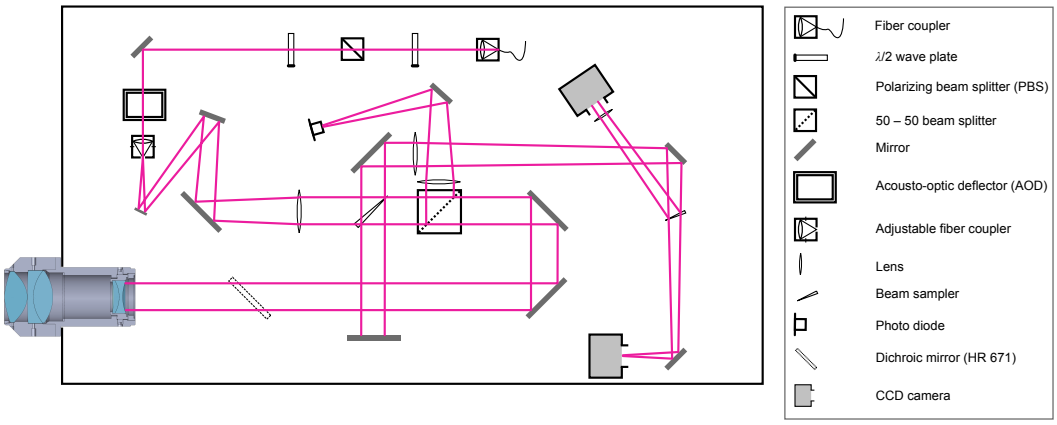

Figure 4.1: Schematic of the breadboard of the new setup. The specifications of the optical components are given in appendix B.

third mirror between the two lenses are used to align the position and angle of the beam relative to the $f = 300\,\text{mm}$ lens. To change the collimation of the telescope, the mount of this lens can be moved along a rail. Optimally, the beam after the telescope is collimated, but it can also be adjusted to be slightly convergent or divergent. This will shift the focal plane behind the objective closer or farther away, respectively, which can be utilized to optimize the overlap of the microtraps with the dipole trap reservoir along the axis of the microtrap beam.

After the telescope, the beam passes through a 2″ beam sampler which deflects 4% of the beam into the diagnostics arm. Two cameras monitor the beam profile and the foci of the $f = 18\,\text{mm}$ lens. The rest passes through a 2″ 50/50 beam splitter onto two mirrors which are used to direct the beam through a dichroic mirror towards the objective. The light which has been reflected by the 50/50 beam splitter is guided onto a photodiode for the stabilization of the overall laser power (see section 5.2).

The beam sampler is a key element of an interferometer together with a silver mirror in the short arm and a dichroic mirror which is placed on the case of the objective. The interferometer is used to align the objective perpendicular to the incoming laser beam which is essential for the quality of the foci.

The alignment procedure is described in more detail in the appendix B.

4.2 The new objective

4.2.1 Design

The objective has been designed with three main goals: small focus size, high numerical aperture and optimum operating conditions for 671 nm and 1064 nm light. The target for the focus was to create a waist $w_0 \approx 0.8\,\mu\text{m}$ which is significantly

smaller than the current one ($w_0 \approx 1.3\,\mu$m nominally, $1.8\,\mu$m as calculated from the measured trap frequencies [Ser11a]). This leads to a larger separation of trap levels and probably to a more reliable preparation of the few-fermion systems (see section 2.3.1). However, it also means that the trap now is less elongated, its aspect ratio (eq. 2.30) is expected to be $\eta \approx 3$ compared to $\eta \approx 10$ in the current setup. As a consequence we expect a more complex energy level scheme where the coupling of radially excited states to the axial spilling force will have to be determined. The aspect ratio may be increased by reducing the waist of the collimated beam entering the objective at the cost of a larger focus size.

In order to detect the atoms by fluorescence imaging, the objective has been designed to have a high numerical aperture NA = 0.6 for light with a wavelength of 671 nm (currently NA = 0.27). It can collect 10% of the emitted photons which leads to a better contrast of the fluorescence images. Also, a higher NA increases the resolution assuming that the objective is diffraction limited. In this case, the Rayleigh criterion specifies the resolution as the distance between the central intensity maximum and the nearest minimum of the point spread function:

$$r = \frac{0.61\lambda}{\mathrm{NA}} \tag{4.1}$$

Its high resolution at $\lambda = 671\,\mathrm{nm}$ of $r = 680\,\mathrm{nm}$ allows it to probe atoms in separate microtraps or maybe even in separate sites of a 1064nm standing wave optical lattice.

From the previous paragraphs it is clear that the objective has to be able to operate with both 671 nm light for imaging and 1064 nm light for trapping. Additionally, we want to switch between the trapping and imaging mode effortlessly. This design goal was addressed by choosing the glasses of the lenses such that the chromatic aberrations for the whole objective are minimized for those wavelengths. Ideally, this would mean that the focal length is identical in both cases. The expected focal shift from simulations was $\Delta f < 1\,\mu$m.

The reason why there were no objectives commercially available for these requirements is that the focal length has to be long enough to overlap the microtrap and the dipole trap in the vacuum chamber. An objective fulfilling the aforementioned requirements with a focal length of approximately 20 mm has been designed in [Ser11a]. It consists of a small achromatic doublet (N-BK7, N-SF11 glasses), a large achromatic doublet (N-SF66, N-PK51) and an asphere (N-FK5). Their positioning in the casing of the objective can be seen in figure 4.1. The small achromat increases the numerical aperture of the objective while maintaining the beam radius at the entrance, effectively acting as an (achromatic) telescope together with the large achromat. The large achromat's purpose is to correct the system for its two operating wavelengths. The asphere focuses the beam while correcting for the vacuum window. The nominal parameters are summarized in table 4.1. Unfortunately, it is mechanically incompatible with the magnetic field coils at the position where it will be mounted. This necessitated the design and construction of new field coils.

wavelength	1064 nm	671 nm
focal length	20.3 mm	
image distance	∞	
diameter field of view	200 μm	
max. diffraction limited NA	0.6	
entrance aperture diameter at max NA	24.4 mm	
resolution	1.08 μm	0.68 μm
waist of focus	0.72 μm	0.45 μm

Table 4.1: Design parameters of the objective from [Ser11a].

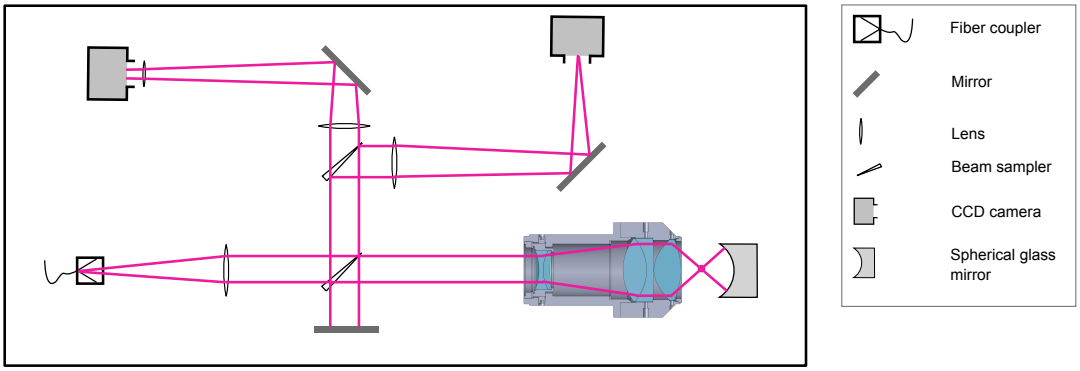

Figure 4.2: Schematic of the Michelson interferometer with one spherical mirror.

4.2.2 Tests

With an interferometer (fig. 4.2) the wavefront of both copies 'BA1001' and 'BA1002' of the objective have been tested at 1064 nm and 671 nm. The key element of the interferometer is the concave spherical mirror which was also produced by Jenoptik. It is placed behind the focus in such a way that the light is reflected perpendicularly on its surface and traces the same way back through the objective. Assuming that the sphere and the other optical elements are perfect, figure 4.3 shows how much the wavefront is distorted by the objectives. Between neighboring light and dark regions, there is a path difference of $\lambda/2$. 'BA1002' distorts the wavefront slightly less than 'BA1001': for a single pass through the objective, the difference over the entire beam profile of 24 mm diameter at $\lambda = 1064$ nm is less than $\lambda/4$.

In order to check the shape and size of the focus, its reflection off the sphere is imaged on a CCD-camera with a $f = 762.5$ mm lens. The magnification of this system is $M = 762.5/20.3 \approx 37.6$. A profile of the focus is fitted with a Gaussian (fig. 4.4a). The resulting waist is $w_0 = 0.94\,\mu$m at 1064 nm. For 671 nm the waist is approximately 1.5 times larger, but the rings around the focus suggest that this might have been caused by, e.g., alignment errors.

The resolution was measured by illuminating a pinhole of approximately 800 nm

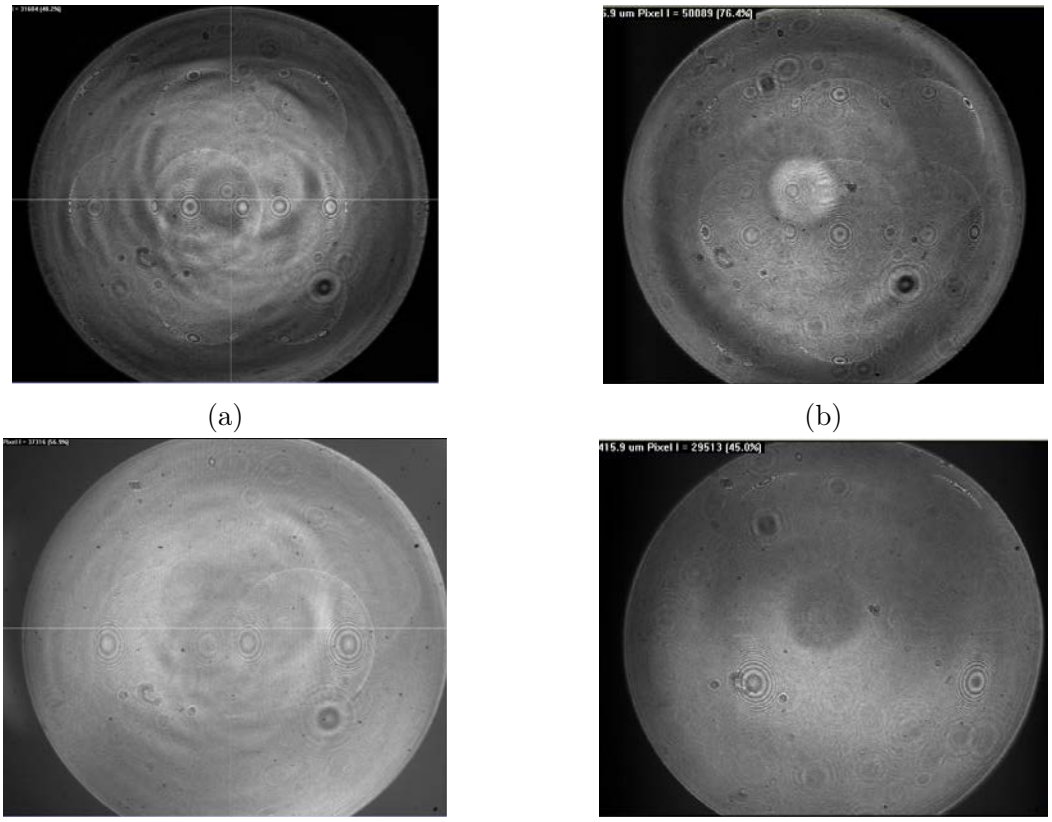

(a) (b)

(c) (d)

Figure 4.3: Wavefront measurements with the interferometer of the 'BA1001' (left) and 'BA1002' (right) objective at 671 nm (top) and 1064 nm (bottom). The entrance aperture of the objective was between 22.4 mm and 24 mm. The path difference between light and dark regions is half a wavelength. Note that the light passes twice through the objective, doubling the wavefront errors on the pictures.

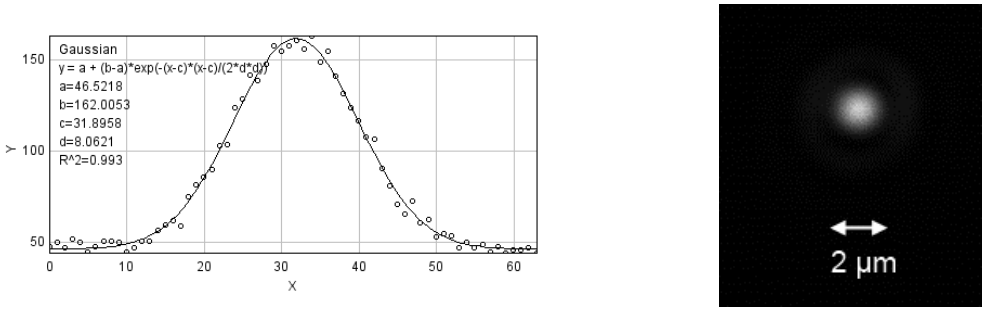

(a) (b)

Figure 4.4: (a) Fit of the profile of the focus created by the sphere. x-axis in units of pixels (pixel size 2.2 μm), y-axis in arbitrary units. (b) Focus of the objective imaged with the microscope objective.

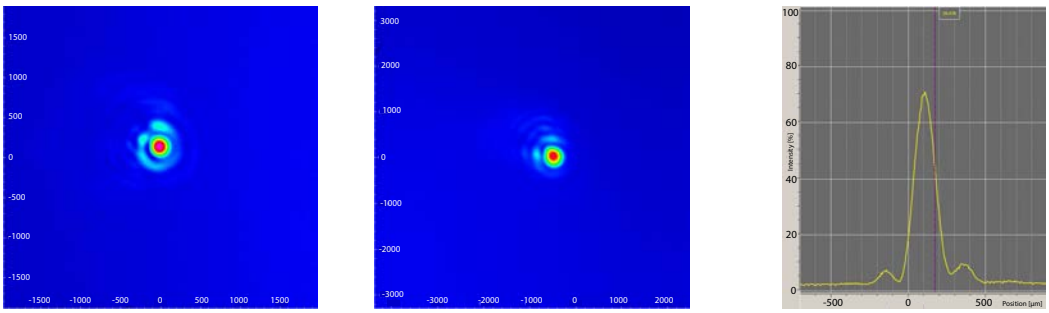

(a) (b) (c)

Figure 4.5: Point spread functions of a pinhole imaged with the 'BA1002' objective for 671 nm (a) and 1064 nm light (b). The magnification of the imaging system was $M = 160 \pm 5$. (c) shows the profile of (a) in y-direction. The units are in μm.

	$\lambda = 671$ nm	$\lambda = 1064$ nm
x-profile	1.08 ± 0.07	1.48 ± 0.09
y-profile	1.05 ± 0.04	1.59 ± 0.11
nominal	0.68	1.08

Table 4.2: Resolution of objective 'BA1002' in μm.

diameter from behind and imaging it directly with the objective. The pinhole was placed slightly farther away from the objective than the focal length (20.3 mm) leading to an image of the pinhole on the CCD camera 332 cm behind the objective. The resulting magnification was $M = 160 \pm 5$. The resolution was determined from distance d of the first minimum from the central maximum of the image of the pinhole (figure 4.5):

$$r_{\text{exp}} = \frac{d}{M}. \tag{4.2}$$

The resolutions for 671 nm and 1064 nm light were extracted from the profiles in two directions (table 4.2). The measured values are significantly larger than the expected theoretical values. We suspect that this is partly due to the finite size of the pinhole which is close to the resolution of the objective. Especially for the wavelengths smaller than the size of the pinhole, a portion of the light would pass through the pinhole undiffracted. This would lead to a smaller effective NA and thus to a larger resolution according to equation (4.1). Another reason for the deviation from the nominal values could be manufacturing errors of the objective. This is supported by the fact that the structures visible in figure 4.5 did not change qualitatively for different alignments of the optical components.

The field of view was tested later in the main setup by tuning the AOD from minimum to maximum deflection. The focus was imaged with a microscope objective (CVI Melles Griot 04OAS016) with a magnification $M = 39.6$ (figure 4.4b). The

waist of the focus varied between $w_0 = 0.94\,\mu$m and $w_0 = 1.00\,\mu$m. The focus shift was also measured with this setup by shining in a collimated $\lambda = 671$ nm beam via the dichroic mirror. The value was $(40 \pm 5)\ \mu$m which is not compatible with the simulated values of $< 18\,\mu$m [Ser11a]. However, this should not be a problem if the imaging optics for the 671 nm light are slightly adjusted.

5 Radio frequency setup and acousto-optic deflector

5.1 Theory of acousto-optics

Devices utilizing acousto-optic effects such as an acousto-optic modulator (AOM) play an important role in optics and information technology. In essence, they consist of a piezo-electric transducer, a medium such as flint glass and an acoustic absorber. The transducer and the absorber are attached to the medium on opposite sides. The transducer induces acoustic vibrations in the medium when it is driven by a RF signal. The absorber prevents the signal from reflecting off the side of the medium and hereby suppresses standing waves. The physics of acousto-optics can be described by the means of wave optics. This section will explain the basic theory of acousto-optics (cf. [Sal91]) and the diffraction of light when multiple sound waves are involved [Hec77].

An acoustic wave is a propagating density modulation in a medium. It is characterized by its velocity v_s, frequency $f = \Omega/(2\pi)$, wavelength $\Lambda = v_s/f = 2\pi/q$ and its intensity I_s. An acoustic plane wave leads to a strain

$$s(x,t) = s_0 \cos(\Omega t - qx) \tag{5.1}$$

in the medium with the amplitude $s_0 = \sqrt{\frac{2I_s}{\rho v_s^3}}$ which depends on the acoustic intensity I_s and the mass density ρ of the medium. The refractive index n of the medium is perturbed by

$$\Delta n(x,t) = -\frac{1}{2} p n_0^3 s(x,t) = n_1 \cos(\Omega t - qx). \tag{5.2}$$

The photoelastic constant p is a phenomenological value, typically of the order 0.1. It can be used to define the acousto-optic figure of merit $M = \frac{p^2 n^6}{\rho v_s^3}$ which allows us to write the perturbation of the diffractive index as $n_1 = \sqrt{M I_s/2}$.

The periodically modulated refractive index $n(x,t) = n_0 - \Delta n(x,t)$ acts as an optical grating on light waves propagating through the medium (figure 5.1). For experiments it is important to know with which efficiency the incident light is diffracted into the different orders. This problem can be treated with coupled-wave theory where we calculate the total electrical field of the incident and diffracted light. In the following, we will work in the xz-plane and neglect the unit vector of the electrical field pointing in the y-direction, keeping only the complex amplitude E. It has to fulfill the wave equation for a inhomogeneous medium [Sal91]

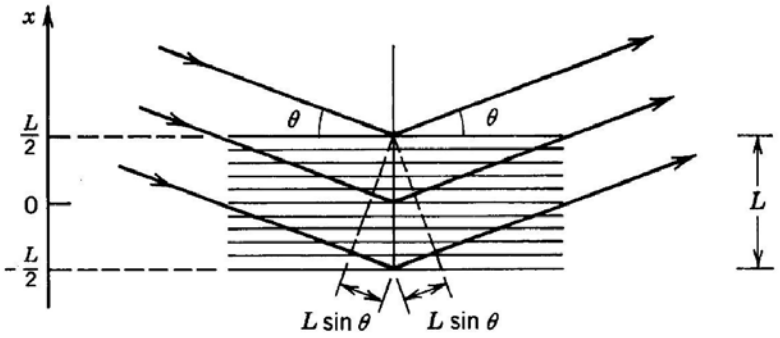

Figure 5.1: Reflection of a optical plane wave on a periodically inhomogeneous medium. From [Sal91]

$$\nabla^2 E - \frac{1}{c^2}\frac{\partial^2 E}{\partial t^2} \approx -S \tag{5.3}$$

with the radiation source

$$S = -\mu_0 \frac{\partial^2 \Delta P}{\partial t^2} = -2\frac{n}{c_0^2}\frac{\partial^2}{\partial t^2}\left(\Delta n E\right) \tag{5.4}$$

which is generated by the perturbation of the polarization density of the medium by the total field E itself. To get an idea of what the source emits, we use the first Born approximation where we assume that the radiation source is created only by the incident plane wave $E_i = A_i \exp\left(i\left(\omega_i t - \boldsymbol{k}_i \cdot \boldsymbol{r}\right)\right)$. Inserting this and Δn from equation (5.2) into the previous equation, we get

$$S = -\frac{n_1}{n}\left(k_+^2 A e^{i(\omega_+ t - \boldsymbol{k}_+ \cdot \boldsymbol{r})} + k_-^2 A e^{i(\omega_- t - \boldsymbol{k}_- \cdot \boldsymbol{r})}\right) \tag{5.5}$$

with $\omega_\pm = \omega \pm \Omega$, $\boldsymbol{k}_\pm = \boldsymbol{k} \pm \boldsymbol{q}$ and $k_\pm = \omega_\pm / c$. We see that the source can emit either an upshifted $(+)$ or a downshifted $(-)$ plane wave.

Suppose that the total field which perturbs the medium consists of the incident plane wave and the upshifted plane wave $E = E_{i0}\exp(i\omega_i t) + E_{+0}\exp(i\omega_+ t)$ where E_{i0} and E_{+0} contain the amplitudes and the space-dependent oscillations. Then the source gives us

$$S = S_+ e^{i\omega_i t} + S_i e^{i\omega_+ t} + \text{terms of other frequencies} \tag{5.6}$$

where $S_{i/+} = -k_{+/i}^2 (n_1/n) E_{i/+0}$. Substituting this result into equation (5.3), we see from comparing the terms of equal frequency that E has to fulfill the coupled Helmholtz equations (mode equations)

$$\begin{aligned}\left(\nabla^2 + k_i^2\right) E_{i0} &= S_+ \\ \left(\nabla^2 + k_+^2\right) E_{+0} &= S_i.\end{aligned} \tag{5.7}$$

In order to solve these equations, we restrict ourselves to small angles $\theta \ll 1$ where the incident wave and the diffracted wave $\boldsymbol{k}_i \approx \boldsymbol{k}_+ \equiv \boldsymbol{k}$ both run approximately parallel to the z-axis. Hence we can replace the electrical fields with $E_{i0} = A_i \exp(-ikz)$ and $E_{0+} = A_+ \exp(-ikz)$. Assuming that the second derivative of A is small compared to $k\partial A/\partial z$ (slowly varying envelope), the mode equations become

$$\begin{aligned} \frac{dA_i}{dz} &= \frac{i}{2} k \frac{n_1}{n} A_+ \\ \frac{dA_+}{dz} &= \frac{i}{2} k \frac{n_1}{n} A_i. \end{aligned} \tag{5.8}$$

We can solve this set of equations by substituting the second equation into the differentiated first equation. Using the boundary condition $A_+(0) = 0$, which states that no light has been diffracted yet at the position where the light enters the medium, one finds the solutions

$$\begin{aligned} A_i(z) &= A_i(0) \cos\left(\frac{V}{2}\frac{z}{d}\right) \\ A_+(z) &= iA_i(0) \sin\left(\frac{V}{2}\frac{z}{d}\right). \end{aligned} \tag{5.9}$$

$V = kn_1 d$ expresses the normalized modulation of the index of refraction which is proportional to $\sqrt{I_s}$. The intensity which is reflected in a medium of length d (i.e. the diffraction efficiency) is

$$R = \frac{|A_+(d)|^2}{|A_i(0)|^2} = \sin^2\left(\frac{Vz}{2d}\right) = \sin^2\left(\frac{\pi L}{\lambda_0 \sin\theta}\sqrt{\frac{M}{2}}\sqrt{I_s}\right). \tag{5.10}$$

In the last step we used $d = L/\sin\theta$ and $n_1 = \sqrt{MI_s/2}$. The reflectance depends on the square root of the intensity of the sound wave I_s, which for small values leads to $R \propto I_s$ (figure 5.2a).

So far, we have only discussed the acousto-optics with a single sound wave in one dimension. As we want to create multiple diffracted beams in the experiment, we will have to operate the AOD with multiple acoustic waves of different frequencies simultaneously. The theory of multimode acousto-optics is explained in detail in [Hec77]. In general, we have N acoustic signals with similar frequencies which modulate the diffraction index of the medium by

$$\Delta n(x,t) = \sum_{j=1}^{N} n_j \sin(\Omega_j t - q_j x + \delta_j) \tag{5.11}$$

where the index j denotes the quantities of the j^{th} acoustic signal and δ_j is its phase. Our total electric field now has the form

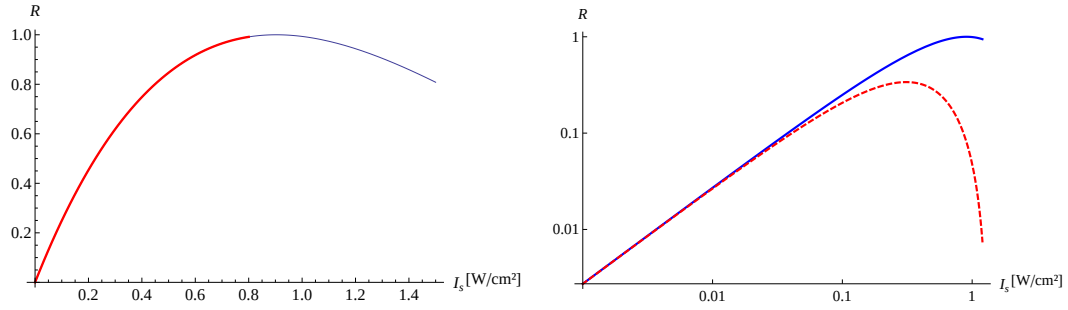

(a) (b)

Figure 5.2: (a) Intensity reflectance R depending on the acoustic intensity I_s for SF6 dense flint glass [Esc75]. The approximate operating window of our AOD is shown in red.[1](b) Intensity reflectance of one of the two beams when the AOD is driven with two acoustic signals of intensity I_s each (red). For comparison, the reflectance from (a) is shown in blue.

$$E = e^{i\omega t} \sum_{m_1=-\infty}^{\infty} \sum_{m_2=-\infty}^{\infty} \cdots \sum_{m_N=-\infty}^{\infty} A_{(\overline{m})} \exp\left(i \sum_{j=1}^{N} m_j(\Omega_j t + \delta_j) - i\boldsymbol{k}_{\overline{m}} \cdot \boldsymbol{r} \right). \quad (5.12)$$

The first sums over $m_1 \dots m_j \dots m_N$ express that the incoming plane wave can be scattered m_j times by any of the sound waves j, where m_j can be any integer number. Every possible scattering process can be described by its set of m_j, $(\overline{m}) = (m_1, m_2, \dots, m_N)$, meaning that the incident wave was scattered m_1 times off sound wave 1, m_2 times off sound wave 2, etc.[2] The amplitude $A_{(\overline{m})}$ depends on this set of scatterings. The total number of scatterings $D_{(\overline{m})} = \sum_{j=1}^{N} |m_j|$ is called the interaction order, terms of higher interaction order usually have a smaller amplitude. This is in contrast to the diffraction order, where terms of different interaction order are grouped based on their diffraction angle: $G_{(\overline{m})} = \sum_{j=1}^{N} m_j$. In the last exponential of equation (5.12), the angular frequency and the wave vector of the scattered light are taken into account, where $\boldsymbol{k}_{\overline{m}} \cdot \boldsymbol{r} = \boldsymbol{k}_i \cdot \boldsymbol{r} + \sum_{j=1}^{N} m_j q_j x$. After inserting E into the wave equation, the coupled mode equations become

$$\left(\frac{d}{dz} - i\Delta K_{(\overline{m})} \right) A_{(\overline{m})} = \sum_{j=1}^{N} \frac{V_j}{2d} \left(A_{(\overline{m}+\overline{a}_j)} - A_{(\overline{m}-\overline{a}_j)} \right). \quad (5.13)$$

If we choose the Bragg angle θ_B for the first diffracted order as our incidence angle θ, the wavevector mismatch ΔK is very large except for the zeroth and first diffraction order (figure 5.3). Therefore, terms where $G \neq 0$ or 1 can be neglected and the mode equations become

[1] Note that the manufacturer of the AOD hasn't reported the exact type of dense flint glass used in the AOD.

[2] One can also regard this process as the absorption and emission of phonons by the photon.

$$\frac{d}{dz}A^0_{(\overline{m})} = \sum_{j=1}^{N} \frac{V_j}{2d} A^1_{(\overline{m}+\overline{a}_j)} \tag{5.14a}$$

$$\frac{d}{dz}A^1_{(\overline{m})} = -\sum_{j'=1}^{N} \frac{V_j}{2d} A^0_{(\overline{m}-\overline{a}_{j'})} \tag{5.14b}$$

where the superscript indicates the diffraction order and $V_j = k_i n_j d/\cos\theta$ similar to the previous case with only one acoustic signal. All sets of $(\overline{m})$ which result in $G_{(\overline{m})} = 0$ and $G_{(\overline{m})} = 1$ respectively are allowed.

For $N = 2$, which in our experiment would result in a double well potential of two microtraps, there are known analytic solutions [Hec77]:

$$A^0_{(m,-m)} = \sum_{r=0}^{\infty} a_{mr} z^r \tag{5.15a}$$

$$A^1_{(m,-m+1)} = -\sum_{r=0}^{\infty} \left(\frac{-1}{r+1}\right) \left(\frac{V_1}{2d} a_{(m-1)r} \frac{V_2}{2d} a_{mr}\right) z^{r+1} \tag{5.15b}$$

with the coefficients

$$a_{mr} = \sum_{s=0}^{\lfloor r/2-|m|/4 \rfloor} C_{mrs} \frac{(-1)^{r/2}}{r!} \left(\frac{V_1 V_2}{4d^2}\right)^{2s+|m|} \left(\frac{V_1^2+V_2^2}{4d^2}\right)^{r/2-|m|-s} \quad \text{and} \tag{5.16}$$

$$C_{mrs} = \frac{(r/2)!}{(r/2-|m|-s)!(s+|m|)!s!}. \tag{5.17}$$

$\lfloor x \rfloor$ denotes the floor of x. In the case of equal acoustic intensities $V_1 = V_2 = V$, the amplitudes can be expressed by Bessel functions of the first kind:

$$A^0_{(m,-m)} = (-1)^m J_{D_{(m,-m)}}(V) \tag{5.18a}$$

$$A^1_{(m,-m+1)} = (-1)^{m+1} J_{D_{(m,-m+1)}}(V). \tag{5.18b}$$

In any case, the reflectance for the incident beam to interaction order $(\overline{m})$ is

$$R = \frac{\left|A_{(\overline{m})}(d)\right|^2}{\left|A_{(\overline{0})}(0)\right|^2}. \tag{5.19}$$

For two equal amplitude acoustic signals, this becomes

$$R = \frac{\left|A^1_{(1,0)}(d)\right|^2}{\left|A_{(\overline{0})}(0)\right|^2} = \frac{\left|A^1_{(0,1)}(d)\right|^2}{\left|A_{(\overline{0})}(0)\right|^2} = \left|J_1(V)\right|^2. \tag{5.20}$$

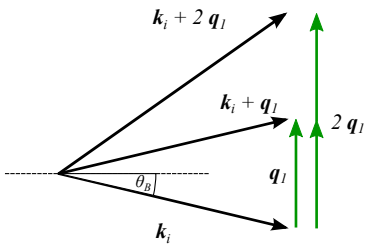

Figure 5.3: Bragg condition for the first diffraction order. The absolute momenta $|\boldsymbol{k}_i|$ and $|\boldsymbol{k}_i + \boldsymbol{q}_1|$ match, other orders are suppressed due to momentum mismatch.

for the first interaction order. The result is shown in figure 5.2b.

The previous results are suited for estimating the diffraction efficiencies for a chain of N microtraps. Even for a perfect AOD, the sum of the intensities of the principal diffracted orders $\sum_j \left|A^1_{(\bar{0}+\bar{a}_m)}\right|^2$ will not add up to one because of intermodulated diffraction orders. For example, for two equal signals, each of the principal diffracted orders has a maximum efficiency $R = 0.339$. Intermodulated orders consist of light with a interaction order which is higher than the diffraction order. For example, if the light absorbs two quanta of the first sound wave and emits one of the second sound wave, it will be in the first diffraction order even though it has scattered three times. However, the intensity of intermodulated orders like $\left|A^1_{(2,-1)}\right|^2 = |J_3(V)|^2$ of the aforementioned example stays at least 2 orders of magnitude below $\left|A^1_{(1,0)}\right|^2$. This should be unproblematic for experiments with two microtraps, but if more than two acoustical frequencies are used, the intermodulated microtraps could overlap with the principle microtraps, deteriorating the potential. In that case, one has to find a compromise between high diffraction efficiency for the principle orders and low diffraction efficiency for the intermodulated orders.

As we use a 2-axis AOD, naturally, we want to diffract the incident light in both axes simultaneously in order to create two-dimensional arrays of microtraps. For this diffraction problem, there are no theoretical solutions available. In [Qid91], the coupled mode equations are derived by generalizing the ansatz of [Hec77]. Unfortunately, they were only solved in the Raman-Nath regime for thin acousto-optical devices which does not apply to our AOD. In order to describe the two-dimensional diffraction of our AOD, it is probably most practical to map the diffraction efficiencies experimentally for the required values.

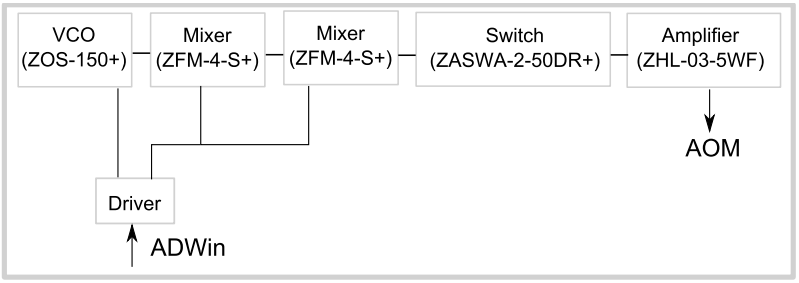

Figure 5.4: RF setup of the control loop for the power stabilization of the laser. In parentheses are the designations of the components from Minicircuits. From [Ser11a].

5.2 Power stabilization of the laser

For the deterministic preparation of few atoms, the stability of the microtrap depth is crucial. Therefore a stabilization control loop for the overall laser power has been implemented using an AOM. The first diffracted order is coupled into a fiber which leads to the main setup. Its diffraction efficiency can controlled through the RF power with which the AOM is driven. The RF power can be adjusted by tuning DC control voltage of the mixers (fig. 5.4). We use two mixers to obtain a larger dynamical range of the RF power. The feedback signal is gathered by a photodiode after the AOD in the main setup (figure 4.1). It is processed with the ADWin control of the main experiment [Ott10]. In order to provide optimal sensitivity of the AOM, it is operated in the linear regime. The stability of the laser intensity is within the measuring resolution of the ADWin (0.3 mV) which is better that 1‰.

As shown in [Ser11a], the old microtrap needed a stability of $< 0.6\%$ to guarantee a preparation fidelity of 99.5%. For the new microtrap a stability on the order of several % should be sufficient for the same preparation fidelity, however, keeping the fluctuation low will reduce errors and heating in more complex systems. With the new setup it will be possible to prepare systems with ten or more atoms deterministically, which is the limit for the current setup.

5.3 RF-setup for the AOD

The current RF-setup for the AOD is designed to generate two frequencies independently from each other (figure 5.5). We use two voltage controlled oscillators (VCO) which can generate RF-signals between approximately $25 - 55$ MHz. The frequency is controlled by a $0 - 17$ V DC input from the ADWin. A part of each signal is tapped with a splitter for monitoring. The power of the remaining signals can be controlled separately over a broad range (≈ 40 dB) by attenuating them with two mixers each, similar to the setup for the power stabilization of the laser. The amount of attenuation is controlled with a DC input by the ADWin. The attenuated signals are combined with another splitter (combiner) and amplified by 46 dB. The

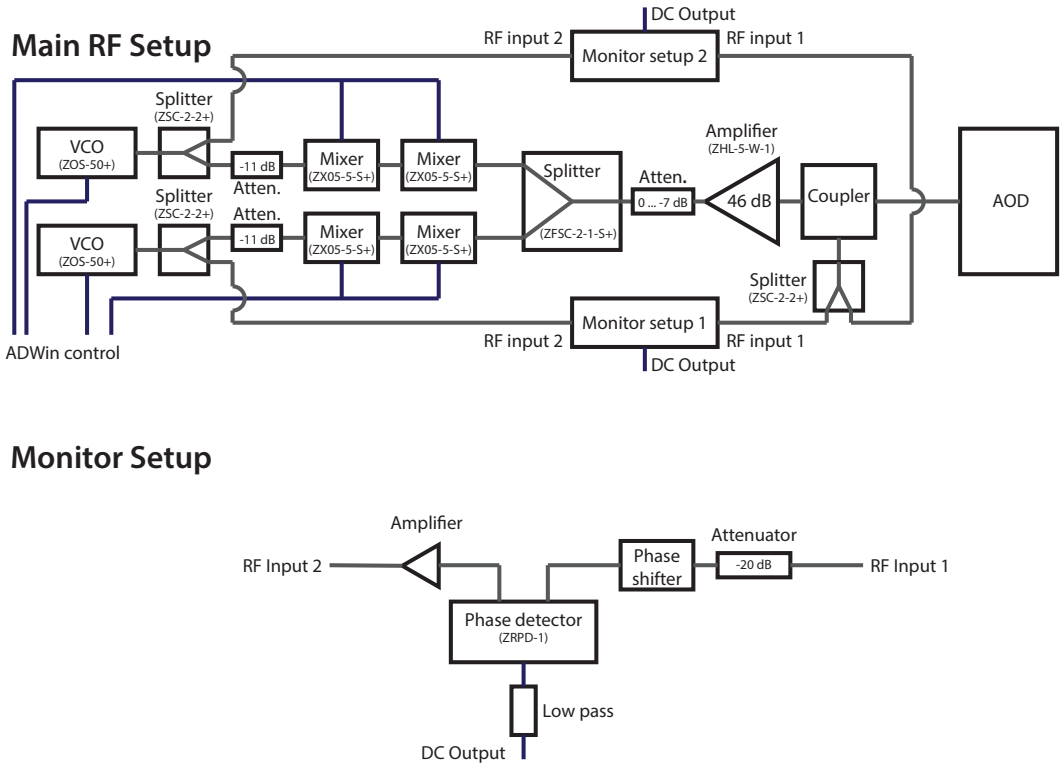

Figure 5.5: Current RF setup for driving the AOD and RF monitoring setup. RF-connections in grey, DC-connections in blue. Minicircuits designations in parentheses.

amplified signal is sent to the AOD.

A coupler between the amplifier and the AOD taps the signal with 30 dB attenuation and sends it to the second port of the monitoring setup. There, the relative amplitude fluctuations can be measured. The phases of both signals are matched with a phase shifter and then combined in a phase detector. The signal which comes from the VCO saturates the phase detector. Consequently, the phase detector's output is essentially a DC signal with the voltage proportional to the amplitude of the signal at the coupler. In order to filter out beats, we send the output signal through a low pass.

The AOD has to fulfill two conditions for a given RF power and frequency: Firstly, the laser power of the diffracted order should be very stable. Secondly, the diffraction angle should be very stable. Hence also the RF powers and frequencies have to be at least equally stable. For future experiments involving tunneling between multiple microtraps, the relative stability of the RF signals is more important than the absolute stability. In order to check the stability, the signal at the coupler was logged for a day (fig. 5.6a). In the first hour after turning on the setup the signal changes until thermal equilibrium, mainly of the amplifier, has been reached. At around 12:00 a.m., both signals have a sharp drop. This is probably caused by the

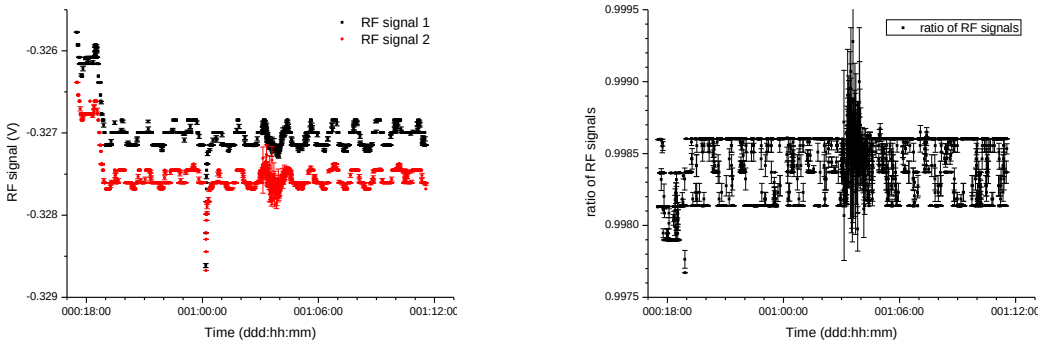

(a) (b)

Figure 5.6: RF signal as measured with the ADWin. Between 5:30 pm and 12:00pm, 10 values were taken every 20 seconds. Each point in (a) is the average over 10 such values, the error bars are the standard errors. In (b) the ratio of the two signals was calculated for every value and then averaged. The error bars again are the respective standard errors. Note that the discrete levels are due to the limited resolution of the analogue to digital converter in the ADWin.

power supply which was unreliable at the time of the measurement. It is not clear why the signals gets a large variation between 03:00 a.m. and 05:00 a.m. A remarkable feature of both RF powers are the oscillations with a period of approximately one hour. It was found out that those oscillations are likely caused by temperature oscillations on the order of 0.1 K caused by the temperature control loop of the laboratory. However, the oscillations do not show in the relative variation of the RF powers (fig. 5.6b), which is stable to less then 1‰ except during the 2 hour period after 03:00 a.m. All in all, the tests show that the RF setup fulfills the stability requirements.

5.4 Tests of the AOD

One of the most important characteristics of the AOD is its response to the frequency and power of the RF setup. As expected, the deflection angle of the beam depends linearly on the frequency generated by the VCO (fig. 5.7a). This was measured by determining the center of the focus on the CCD 2 (figure 4.1, then a Point Grey camera) by means of fitting the profile of the focus with a Gaussian.

The behavior of the diffraction efficiency is more complex. We cannot directly apply the results from the first section of this chapter because our AOD is far from ideal. The power produced by the RF setup which generates the acoustic waves in the AOD strongly depends on the RF frequency. We have measured that the output power of the VCO alone drops by 3 dB when increasing the frequency from 25 MHz

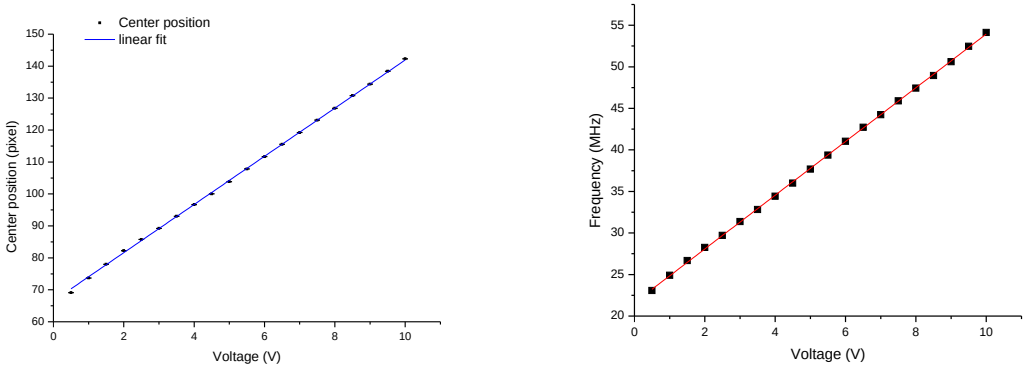

(a) (b)

Figure 5.7: (a) Position of the focus on the CCD 2 (Point Grey, pixel size 3.75 μm, magnification $M \approx 1.67$). The error bars are the fitting errors of the individual Gaussian fits of the focus profiles. The slope of the linear fit $f(x) = a + bx$ corresponds to $b = 8.73\,\mu$m/MHz. (b) Dependence of the VCO frequency on the control voltage. The parameters of the linear fit are $a = 21.6$ MHz and $b = 3.24$ MHz/V.

to 55 MHz. This can cause the RF power at the AOD to vary by 3 dB as well, which corresponds to 50%. We then have to take into account that the RF power which arrives at the AOD is not converted to acoustic waves entirely: The power reflected by the AOD varies by 25 dB depending on the frequency, the maximum being at 5 dBm by typical operating parameters, which lies above the stability requirements of 1‰. Furthermore, a sweep over the RF frequency showed that the reflected RF power oscillates with a period of ca. 100 kHz. Additionally, we do not know how much of the power used by the transducers is converted to sound waves and how much is dissipated.

In order to determine the diffraction behavior of the AOD, the power of the laser beam was stabilized before the AOD. The beam was diffracted only in one direction by one acoustic frequency at a time and the 0^{th} order was blocked. The power of the first order was measured with the photodiode. As can be seen in fig. 5.9a, the efficiency changes at two different scales if the VCO voltage (i.e. RF frequency, fig. 5.7b) is changed. The large scale variation has a period on the order of 1 V VCO voltage, the small scale variation on the order of 10 mV. We suspect that the small variations stem from the reflection of RF power of the AOD, since the structures are similar. If the RF power is changed, the diffraction efficiency does not respond linearly (fig. 5.8b). At low power, the reason probably is the non-linear response of the mixer to the control voltage (figure 5.8a). At high power, the non-linearity could be due to the theoretically predicted saturation of the diffraction efficiency. Since both the RF frequency and the RF power are non-trivial parameters for the diffraction efficiency, a more extensive measurement was performed: The efficiency

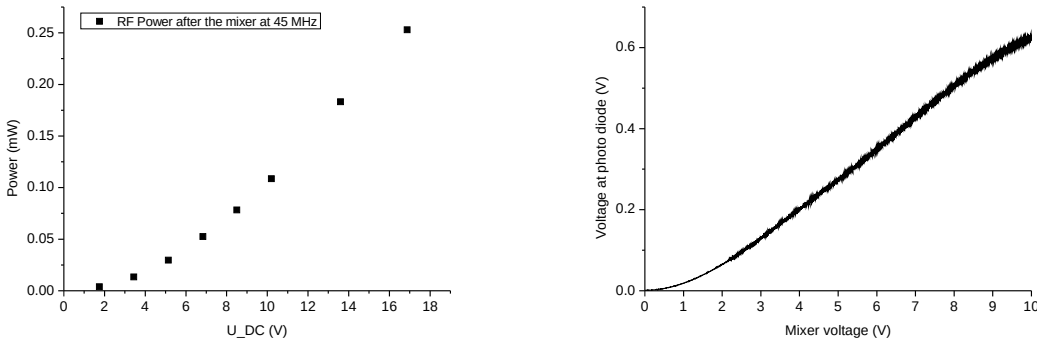

(a) (b)

Figure 5.8: (a) RF power after the mixer at 45 MHz and (b) diffraction efficiency at 30 MHz for different mixer control voltages and constant RF input power.

was measured for 10000 steps in the RF frequency ν_{RF} and 10 steps in the RF power P_{RF} (or, more precisely, in the control voltage of the RF power). It turned out that it could be fitted by a two dimensional polynomial of 9^{th} power in ν_{RF} and 2^{nd} power in P_{RF}:

$$U_{PD} = \sum_{m=0}^{2} \sum_{n=0}^{9} a_{nm} \ (\nu_{RF})^n \, (P_{RF})^m \,, \tag{5.21}$$

where U_{PD} is the voltage measured at the photodiode.

Since the fit only describes the large scale behavior of the efficiency and not the small scale oscillations, the actual data deviate from it by up to 3%. This is not sufficient to control the depth of the microtrap to the desired level of $< 1‰$. Therefore the idea was to implement a lookup table in the control of the AOD in such a way that it calculates the required RF power given a desired RF frequency and diffraction efficiency. However, with measurements for only 10 different RF powers, inverting the data directly would be too rough. For a given frequency, the mixer control voltage is calculated by interpolating it linearly between the nearest two measured frequencies at the nearest measured efficiency value. The same is done for the next nearest efficiency value, resulting in two mixer settings for the desired frequency at the nearest and next to nearest to desired efficiency. The optimum mixer setting is acquired by interpolating between these two values. The exact method for generating the lookup table and interpolating the values can be found in appendix C. A visual representation of the lookup table is shown in figure 5.11.

A sweep with the lookup table activated over the VCO voltage, i.e. RF frequency, shows that, between 2 and 8 V, the large fluctuations of the efficiency are much less pronounced (cf. figure 5.12, figure 5.9a). It is remarkable that in spite of the fine sampling of the lookup table, the smaller oscillations are still visible with an

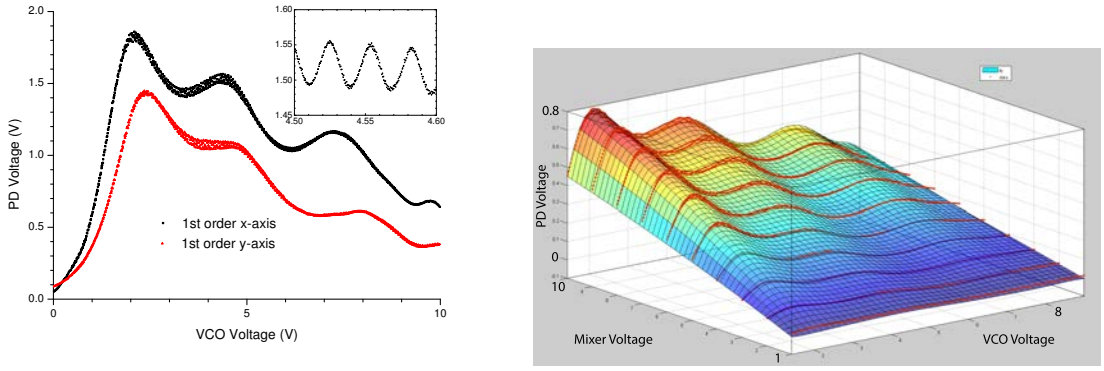

(a) (b)

Figure 5.9: (a) Frequency response of the AOD for the diffraction of a laser beam in x and y directions seperately. The inset shows a detail of the curve. For sake of clarity, only $1/20^{\text{th}}$ of the measured values are displayed. (b) Laser intensity (PD voltage) for 10 RF powers (mixer voltage) and 2000 RF frequencies (VCO voltage), shown as red points. The fitted polynomial (eq. (5.21)) is shown as a surface. Brighter data points lie above the fit surface, darker data points lie below.

amplitude of at least 1%. One possible explanation is that in the days between the measurement of the lookup table and the test of the lookup table, the frequency of the VCO could have drifted, e.g., due to temperature changes. Therefore, one might get better results once the lookup table is retaken when the RF setup has been installed on a temperature stabilized mount. Even if the small oscillations cannot be eliminated, that would not restrict experiments where the positions of the microtraps (RF frequencies) are constant. In these cases, the diffraction efficiency can by fine-tuned by fitting the images of the foci from the diagnostics camera. An image of four foci with typical, uncorrected intensities is shown in figure 5.10.

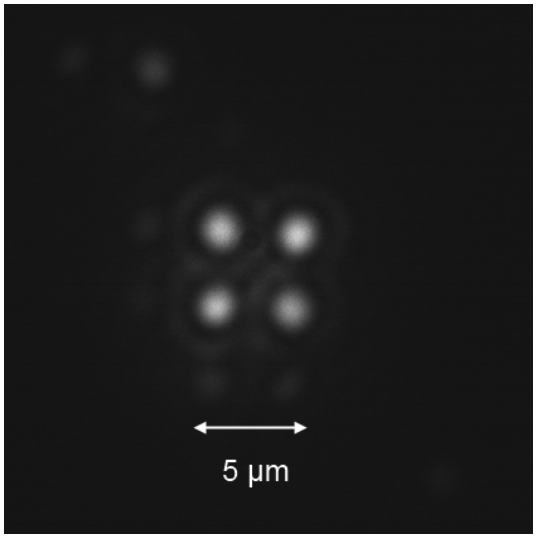

Figure 5.10: Grey scale image of four foci created with two RF-signals each for the x- and y-directions at the AOD. The other features are likely to be intermodulation orders from the AOD or reflections in the optical setup.

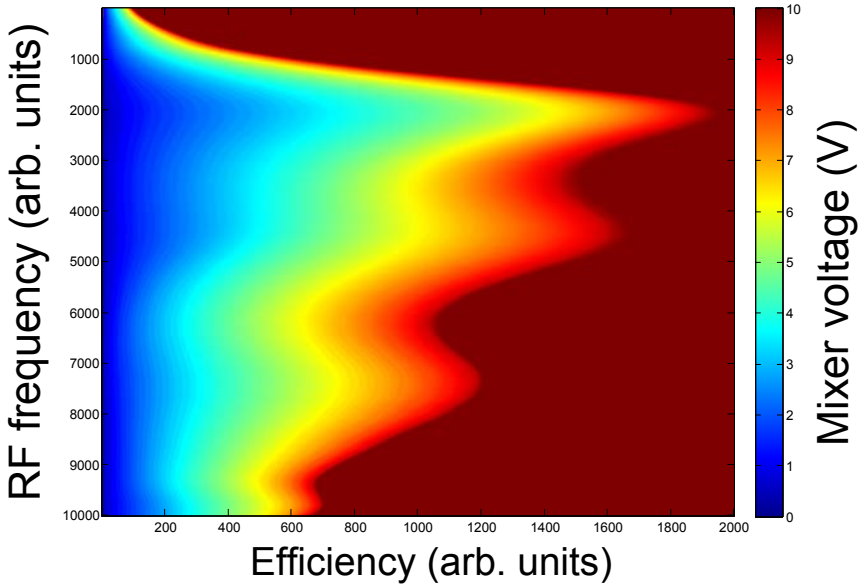

Figure 5.11: Lookup table for the AOD: required mixer voltage (color map) vs. efficiency and RF frequency. If the desired efficiency cannot be reached, the mixer stays at its maximum voltage (10 V).

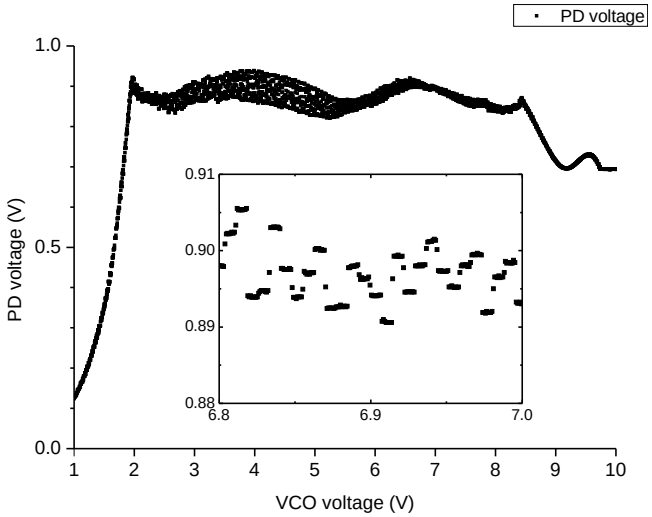

Figure 5.12: Frequency response of the AOD with the lookup table implemented. At the edges, the diffraction efficiency could not be maintained as the maximum RF power had been reached. The inset shows a detail of the main graph.

6 Conclusion and outlook

During this thesis, an apparatus was built which will enable the existing few-fermion experiment to produce complex potential landscapes. The tests of this new setup, in particular of the AOD and the new objective, show that it is able to create the potentials with the required stability. The tunneling and interaction parameters of the system can by tuned via the potential and the interaction strength over several orders of magnitude.

The next step will be to put the new setup into operation at the experiment. Before it can be installed, the old magnetic field coils of the experiment have to be replaced. This entails a readjustment of the MOT and the dipole trap. With the new setup in place, we have to overlap the position of the microtraps with the dipole trap. Our preparation procedure of few-fermion systems in a single microtrap will have to be reevaluated as the energy levels of the new microtrap have to be mapped out. This will also allow us to determine the size and shape of the single microtraps.

Once these tests are completed, we can start studying multiple well potentials. We will have to determine which preparation scheme is best for reaching the ground state of a multiple well potential. The possibilities include preparing a single microtrap and then allowing tunneling between microtraps or preparing multiple microtraps simultaneously. At first, we will start working with a double well potential, where we can check the agreement between the experiment and the theoretical results of this thesis. Later, we can explore the phase diagrams of various potential landscapes for different interaction strengths, potential depths, atom numbers, population imbalances, etc. One of the simpler potentials would be a square array of four microtraps (cf. figure 5.10), which with the right parameters could simulate either a square plaquette of a 2D lattice or a linear chain with periodic boundary conditions. Another line of study are time averaged potentials. We can create, e.g., time averaged two-dimensional potentials if we modulate the position of the microtraps at a much faster time scale than the trapping frequency. For example, we could then investigate the transition between 1D and 2D systems dynamically.

In order to create more complex potentials, we will have to expand the RF control of the AOD. If we increase the number of simultaneous RF frequencies, this will enable us to create large square arrays of up to 10×10 microtraps. However, a practical solution has to be found to control the diffraction efficiency of the AOD over the entire frequency range. This may be achieved by optimizing the lookup table presented in this thesis. With large arrays of microtraps, we could research the transition from finite lattices to infinite lattices. Combining this approach with time averaged potentials, we could also create different lattice geometries, e.g., a triangular lattice, by projecting the potential 'line by line'.

Another promising perspective would be manipulating single sites of an array. One could for example artificially impose noise on the microtrap array or alter the potential of specific sites, mimicking defects in solids. Also, one could use the single site control to selectively release atoms of a certain spin state on certain sites from the trap. This could be used to measure the distribution and the order of the atoms in a lattice or to perform studies on quantum information technology.

All in all, the methods described in this section show that few-fermion systems can potentially lead to important contributions in the fields of solid state physics, few- and many-body physics. The setup described in this thesis is one of the initial steps in this direction for our few-fermion experiment.

Appendix

A Numerical calculation of the Hubbard parameters in a double well

Mathematica script for calculating the wavefunctions, eigenenergies and Hubbard parameters of a double well in one dimension. The physical meaning of the parameters is described in chapter 3. The script has been adapted and extended from [Eve10].

```
Remove["Global`*"];

(*Initialization of parameters and variables*)

parameters = {a -> 1., s -> w0/2, P -> 0.1*10^-3, δ -> 0.0,
   Vint -> 4*π*hbar^2/m*asc/at^3};
(*variable experimental parameters: amplitude scale, waist, laser \
power, tilt, interaction energy*)
(*all parameters in SI units*)
d = 0.5*10^(-6);

(*separation of the microtraps*)
setstate = 1; (*energy level (starting from 1)*)
c = 2.99792458 10^8;

(*speed of light*)
kb = 1.380658 10^(-23);      (*Boltzmann's constant*)
hbar = 1.05457266 10^(-34);      (*reduced Planck's constant*)
Γ = 2 π 5.872 10^6;     (*line width*)
m = 6 1.67 10^(-27);     (*mass of Li6*)
λ0 = 671 10^(-9);     (*transition wavelength*)
ω0 = 2 π c/λ0;  (*transition frequency*)
a0 = 5.29177210*10^(-11);(*Bohr radius*)

(*variable experimental parameters*)
asc = 100*a0;      (*scattering length*)
w0 = 0.8* 10^(-6);      (*minimal beam waist (z=0)*)

(*fixed experimental parameters*)
λ = 1064 10^(-9) // N ;    (*trapping wavelength*)
ω = 2 π c / λ;
k = 2 π / λ;
Er = hbar^2 * (2*π / λ)^2 / (2 * m) ;(*recoil energy*)
zr = π w0^2/λ;    (*rayleigh range*)

(*calculate beam intensity*)
I0 = 2 P/(π*
```

```
      w0^2);     (*intensity of one beam in focus, factor 2 b/c of \
Gauss profile*)
(*w[z_]:=w0 Sqrt[1+(z/zr)^2] (*Waists in longitudinal (i.e. vertical) \
direction (z)*)
Intensitymax[z_, P_]:=I0[P]/(Sqrt[(1+(z/zr)^2)*(1+(z/zr)^2)]) \
(*intensity in beam middle as a function of z*)
Intensitybeam[x_,y_,z_, P_]:=Intensitymax[z, \
P]*Exp[-2(x^2+y^2)/w[z]^2] (*intensity in whole beam, for later 3D \
calculations*)*)
V = -3 π c^2/
     2/ω0^3*(Γ/(ω0 - ω) + \
Γ/(ω0 + ω))*
   I0;(*dipole potential, from (B) Eq (10)*)

(* Trapping frequency for a gaussian potential *)
wt = Sqrt[-a*V/s^2/m];
at = (Sqrt[hbar/m/wt] /. parameters);

(*quantities for numerics*)
pStart = -d - w0;
pEnd = d + w0;
pStep = (2*d + 2*w0)/127;
NumPStep = (pEnd - pStart)/pStep // Round
pval[i_] := pStart + i*pStep
dimVec = (NumPStep + 1)
(*___ ___ ___ ___ ___ ___ ___ ___ ___ ___ ___ ___ ___ ___ ___ ___ ___ \
___ ___ ___ ___*)

(*Definition of discretized potential, Hamiltonian HΨ and \
wavefunction Ψ*)

(*Calculate the energies in Hz from here on*)
Potential =
  V/(hbar*2*
       π)*(a*(PDF[NormalDistribution[-d, s], x] + (1 + δ)*
          PDF[NormalDistribution[d, s], x])*Sqrt[2*π]*s - 2*a);
Potential;
% /. parameters;
tmp = %;
Plot[tmp, {x, -d - w0, d + w0},
 PlotRange -> {{-d - w0, d + w0}, {0, -2*a*V/(hbar*2*π)} /.
    parameters}]
HPsi[p_] = -hbar^2/(2*m)/(hbar*2*π)*(Psi[p + 1] + Psi[p - 1] -
        2*Psi[p])/
      pStep^2 + (a*(PDF[NormalDistribution[-d, s],
            pval[p]] + (1 + δ)*
           PDF[NormalDistribution[d, s], pval[p]])*Sqrt[2*π]*s - 2*a)*
    V/(hbar*2*π)*Psi[p];
PsiVector = Table[Psi[p], {p, 0, NumPStep}] // Flatten;
(*___ ___ ___ ___ ___ ___ ___ ___ ___ ___ ___ ___ ___ ___ ___ ___ ___ \
___ ___ ___ ___*)
```

```
(*Finding the eigensystem: Diagonalization of H*)

(*Conversion of the Hamiltonian in matrix form*)
Table[HPsi[p], {p, 0, NumPStep}] // Flatten;
% /. Psi[p_] /; p < 0 -> 0;
% /. Psi[p_] /; p > NumPStep -> 0;
% /. parameters;

CoefficientArrays[%, PsiVector];
HMatrix = %[[2]];
MatrixForm[HMatrix[[1 ;; 5, 1 ;; 5]]]
(* calculate first 25 eigenstates and eigenenergies *)
Eigensystem[HMatrix, -25];
sys = {Reverse[%[[1]]], Reverse[%[[2]]]};
Eigenstates
Eigenstate[i_] := sys[[2, i]]
PsiVal[state_, p_] :=
 If[(p >= 0) && (p <= NumPStep), Eigenstate[state][[p]], 0]
(*plot of three eigenstates and their absolute square*)
state = setstate;
PsiVal[state, (NumPStep + 1)/2](*value of wf on barrier*)
Show[ListPlot[
  Table[Table[{pval[i], PsiVal[state + j, i]}, {i, 0, NumPStep}], {j,
    0, 2}], Joined -> True,
  PlotStyle -> {{Red, Thick}, {Green, Thick, Dashed}, {Black, Thick}}],
 ListPlot[
  Table[Table[{pval[i], PsiVal[state + j, i]^2}, {i, 0,
     NumPStep}], {j, 0, 2}], Joined -> True,
  PlotStyle -> {Red, {Green, Dashed}, Black}]]
state =.
(*checking the orthonormality of the eigenstates*)
Sum[PsiVal[1, p]*PsiVal[1, p], {p, 0, NumPStep}] // Chop
Sum[PsiVal[1, p]*PsiVal[2, p], {p, 0, NumPStep}] // Chop
Eigenenergies
EPsi[i_] := sys[[1, i]];
Efit = Fit[Table[{i, EPsi[i]}, {i, 10, 25}], {1, x, x^2}, x]
(*note: for a harmonic oscillator, the eigenenergies would increase \
linearly*)
Show[ListPlot[Table[{i, EPsi[i]}, {i, 1, 25}],
  PlotStyle -> PointSize[Medium]], Plot[Efit, {x, 1, 25}]]
ListPlot[Table[{i, EPsi[i] - EPsi[i - 1]}, {i, 2, 25}],
 PlotStyle -> PointSize[Medium]]
(*___ ___ ___ ___ ___ ___ ___ ___ ___ ___ ___ ___ ___ ___ ___ ___ ___ \
___ ___ ___ ___*)

(*Summary: Potential, Eigenenergies and Eigenstates*)

Show[
 Plot[Potential - EPsi[1] /. parameters, {x, -d - w0, d + w0},
  PlotRange -> {{-d - w0,
     d + w0}, {0.05*a*V/(hbar*2*π), -0.25*a*V/(hbar*2*π)} /.
     parameters}],
```

```
 Plot[{EPsi[1] - EPsi[1], EPsi[2] - EPsi[1], EPsi[3] - EPsi[1],
   EPsi[4] - EPsi[1], EPsi[5] - EPsi[1], EPsi[6] - EPsi[1],
   EPsi[7] - EPsi[1], EPsi[8] - EPsi[1]}, {x, -d - w0, d + w0},
  PlotStyle -> {Red, Blue, Green, Purple, Black, Black, Black, Black}],
 ListPlot[
  Table[{pval[i], (PsiVal[1, i])*(EPsi[3] - EPsi[1])*2 + EPsi[1] -
     EPsi[1]}, {i, 0, NumPStep}], Joined -> True,
  PlotStyle -> {Thick, Red}],
 ListPlot[
  Table[{pval[i], (PsiVal[2, i])*(EPsi[3] - EPsi[1])*2 + EPsi[2] -
     EPsi[1]}, {i, 0, NumPStep}], Joined -> True,
  PlotStyle -> {Dashed, Thick, Blue}],
 ListPlot[
  Table[{pval[i], (PsiVal[3, i])*(EPsi[3] - EPsi[1])*2 + EPsi[3] -
     EPsi[1]}, {i, 0, NumPStep}], Joined -> True,
  PlotStyle -> {Thick, Green}],
 ListPlot[
  Table[{pval[i], (PsiVal[4, i])*(EPsi[3] - EPsi[1])*2 + EPsi[4] -
     EPsi[1]}, {i, 0, NumPStep}], Joined -> True,
  PlotStyle -> {Thick, Purple}], AxesStyle -> 14,
 AxesLabel -> {"Position [m]", "Energy [Hz]"}, LabelStyle -> 14,
 Frame -> True]
(*_____ _____ _____ _____ _____ _____ _____ _____ _____ _____ _____ _____ _____ _____ _____ _____ \
_____ _____ _____ _____*)

(*Defining a left-right-basis*)

PsiValL[p_] := (PsiVal[1, p] + PsiVal[2, p])/Sqrt[2];
PsiValR[p_] := (PsiVal[1, p] - PsiVal[2, p])/Sqrt[2];
state = 1;
Show[
 ListPlot[
  Table[Table[{pval[i], PsiVal[state + j, i]}, {i, 0, NumPStep}], {j,
    0, 1}], Joined -> True, PlotStyle -> {{Red}, {Green, Dashed}}(*,
  PlotRange->{{pval[0],pval[NumPStep]},{-0.5,0.5}}*)],
 ListPlot[{Table[{pval[i], PsiValL[i]}, {i, 0, NumPStep}],
   Table[{pval[i], PsiValR[i]}, {i, 0, NumPStep}]}, Joined -> True,
  PlotStyle -> {{Black, Thick}, {Blue, Thick}},
  PlotRange -> {{pval[0], pval[NumPStep]}, {-0.5, 0.5}}],
 PlotRange -> {{pval[0], pval[NumPStep]}, {-0.5, 0.5}}]
state =.
(*time evolution of ΨL*)
Psi1[p_, t_] :=
 Exp[-I/hbar*EPsi[1]*t]/Sqrt[2]*PsiVal[1, p] +
  Exp[-I/hbar*EPsi[2]*t]/Sqrt[2]*PsiVal[2, p]
ListPlot[
 Table[{pval[i],
    Psi1[i, 0.001]*Psi1[i, 0.001]* /. parameters}, {i, 1,
    NumPStep}] // Chop, Joined -> True,
 PlotRange -> {{pval[1], pval[NumPStep]}, {0, 0.2}}]
(*_____ _____ _____ _____ _____ _____ _____ _____ _____ _____ _____ _____ _____ _____ _____ _____ \
_____ _____ _____ _____*)
```

```
(*Calculating the Hubbard parameters*)

(*tunneling behavior: how much is left in the left well after a time \
t?*)
Tunnelcomplex[t_] :=
 Sum[Psi1[i, t]**PsiValL[i], {i, 1, NumPStep}]
Tunnel[t_] := Tunnelcomplex[t]**Tunnelcomplex[t]
Plot[Cos[(EPsi[1] - EPsi[2])*hbar*2*π/hbar/2*t]^2 /. parameters, {t,
  0, 2/(EPsi[2] - EPsi[1])}]
J = (EPsi[2] - EPsi[1])/2 (*tunneling parameter*)
U = Vint*
   Sum[PsiValR[i]**PsiValR[i]**PsiValR[i]*
      PsiValR[i], {i, 1, NumPStep}]/(2*π*hbar) /.
  parameters (*on-site interaction*)
UNN = Vint*
   Sum[PsiValR[i]**PsiValL[i]**PsiValR[i]*
      PsiValL[i], {i, 1, NumPStep}]/(2*π*hbar) /.
  parameters (*off-site interaction*)
DJ = Vint*
   Sum[PsiValR[i]**PsiValL[i]**PsiValL[i]*
      PsiValL[i], {i, 1, NumPStep}]/(2*π*hbar) /.
  parameters (*tunneling correction from off-site interaction*)
(*___ ___ ___ ___ ___ ___ ___ ___ ___ ___ ___ ___ ___ ___ ___ ___ ___ \
___ ___ ___ ___*)

(*Calculation of Hubbard parameters for different laser powers*)

(*start from the definitions potential, Hamiltonian and wavefunction \
from above*)
power = 5*10^(-5);
l = 1; (*index*)
(*initialize output lists*)
powerlist = {};
J = {};
U = {};
UNN = {};
DJ = {};
While[power <= 0.004,
 temp = {};
 temp2 = {};
 temp3 = {};
 temp4 = {};
 parameters = {a -> 1., s -> w0/2, P -> power, δ -> 0,
   Vint -> 4*π*hbar^2/m*
     asc/at^3}; (*reinitialize parameters for every iteration*)
 at = (Sqrt[hbar/m/wt] /. parameters);
 temp = Table[HPsi[p], {p, 0, NumPStep}] // Flatten;
 temp2 =
  temp /. parameters /. Psi[p_] /; p < 0 -> 0 /.
   Psi[p_] /; p > NumPStep -> 0;
 temp3 = CoefficientArrays[temp2, PsiVector];
```

```
 HMatrix = temp3[[2]];
 temp4 = Eigensystem[HMatrix, -25];
 sys = {Reverse[temp4[[1]]], Reverse[temp4[[2]]]};
 Eigenstate[i_] := sys[[2, i]];
 PsiVal[state_, p_] :=
  If[(p >= 0) && (p <= NumPStep), Eigenstate[state][[p]], 0];
 PsiValL[p_] := (PsiVal[1, p] + PsiVal[2, p])/Sqrt[2];
 PsiValR[p_] := (PsiVal[1, p] - PsiVal[2, p])/Sqrt[2];
 EPsi[i_] := sys[[1, i]];
 (*append results to output lists*)
 J = Append[J, (EPsi[2] - EPsi[1])/2];
 U = Append[U,
     Vint*Sum[
       PsiValR[i]^*PsiValR[i]^*PsiValR[i]*
        PsiValR[i]/(2*π*hbar), {i, 1, NumPStep}]] /. parameters;
 UNN = Append[UNN,
     Vint*Sum[
       PsiValR[i]^*PsiValL[i]^*PsiValR[i]*
        PsiValL[i]/(2*π*hbar), {i, 1, NumPStep}]] /. parameters;
 DJ = Append[DJ,
     Vint*Sum[
       PsiValR[i]^*PsiValL[i]^*PsiValL[i]*
        PsiValL[i]/(2*π*hbar), {i, 1, NumPStep}]] /. parameters;
 powerlist = Append[powerlist, power];
 power =
  power*1.1;(*calculate next power value, can be exponential or \
linear*)
 l = l++;
 ]
(*plot the output lists*)
ListLogLogPlot[
 Table[{powerlist[[i]]*1000, J[[i]]}, {i, 2, Length[powerlist]}],
 AxesStyle -> 14, AxesLabel -> {Power [mW], J [Hz]}, LabelStyle -> 14,
  Joined -> True, PlotStyle -> Thick]
ListLogLogPlot[
 Table[{powerlist[[i]]*1000, U[[i]]}, {i, 2, Length[powerlist]}],
 AxesStyle -> 14, AxesLabel -> {Power [mW], U [Hz]}, LabelStyle -> 14,
  Joined -> True, PlotStyle -> Thick]
ListLogLogPlot[
 Table[{powerlist[[i]]*1000, UNN[[i]]}, {i, 2, Length[powerlist]}],
 AxesStyle -> 14, AxesLabel -> {Power [mW], Subscript[U, NN] [Hz]},
 LabelStyle -> 14, Joined -> True, PlotStyle -> Thick]
ListLogLogPlot[
 Table[{powerlist[[i]]*1000, -DJ[[i]]}, {i, 2, Length[powerlist]}],
 AxesStyle -> 14, AxesLabel -> {Power [mW], Δ J [Hz]},
 LabelStyle -> 14, Joined -> True, PlotStyle -> Thick]
ListLogLogPlot[
 Table[{powerlist[[i]]*1000, J[[i]]/U[[i]]}, {i, 2,
   Length[powerlist]}], AxesStyle -> 14,
 AxesLabel -> {Power [mW], J/U}, LabelStyle -> 14, Joined -> True,
 PlotStyle -> Thick]
ListLogLogPlot[
```

```
 Table[{powerlist[[i]]*1000, -DJ[[i]]/U[[i]]}, {i, 2,
   Length[powerlist]}], AxesStyle -> 14,
 AxesLabel -> {Power [mW], Δ J/U}, LabelStyle -> 14,
 Joined -> True, PlotStyle -> Thick]
ListLogLogPlot[
 Table[{powerlist[[i]]*1000, -DJ[[i]]/J[[i]]}, {i, 2,
   Length[powerlist]}], AxesStyle -> 14,
 AxesLabel -> {Power [mW], Δ J/J }, LabelStyle -> 14,
 Joined -> True, PlotStyle -> Thick]
```

B Alignment of the optical setup

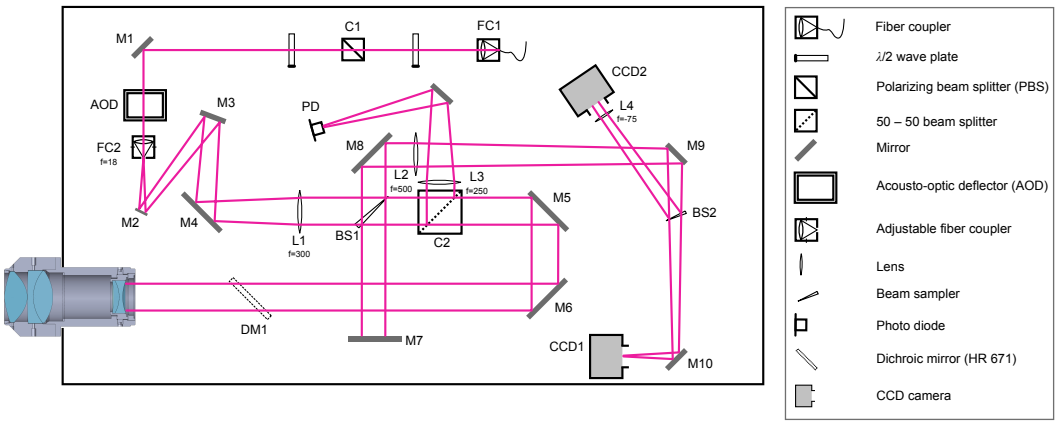

Figure B.1: Optical setup

This appendix summarizes how to efficiently align the new setup. In order to follow the entire procedure, it might be necessary to remove some optical components from the breadboard. The labels used in the description are specified in figure B.1.

- Adjust the beam coming from fiber coupler FC1 through cube C1 onto mirror M1.
- Adjust the height and angle of the beam behind M1 by aligning it through two irises which are at the correct height. The AOD and M2 have to be removed for this step.
- Install the AOD. Check with the powermeter and the IR camera that the beam is not being clipped on either aperture of the AOD.
- Walk the angle of the AOD and M1 in both axes to maximize the intensity of the diffracted order. Check the quality of the beam profile, for example with CCD2.
- Align FC2. The $f = 18\,\mathrm{mm}$ lens must be coaxial with the fiber adapter. This can be achieved by passive alignment with a slip ring.
- Mark the position of the beam after the AOD without FC2. Insert FC2 such that the beam is centered on that position.

- Shift the fiber adapter of FC2 such that only the 1,1 diffracted order passes. Use this order for the further alignment.
- Lock the AOD and M1.
- Align the telescope such that the beam is centered on L1 and passes through it perpendicularly:
  - Use M2 for the position on L1, check it visually, e.g., with an iris.
  - Use M4 for the angle. Use a mirror mounted in an SM tube. Attach it behind L1 on the same lens mount.
  - Try to overlap the incoming and reflected beam by walking M2 and M4.
- Collimate the beam after L1 by using a shear plate:
  - Install a shear plate behind L1 at an angle of approximately 45° sideways.
  - Shift L1 along its rails until the number of interference fringes after the shear plate is minimized (they should then be horizontal).
  - Check the position and angle of the beam on L1 as described previously.
- Lock M2, M3, M4 and L1.
- Position beam sampler BS1 centrally on the beam. If it is off-center, this can be seen with CCD2 on the beam profile.
- Position C2 centrally on the beam.
- Align the interferometer:
  - Install a mirror (e.g., M6) perpendicularly to the beam and overlap the incoming and reflected beams, for instance at FC1. Couple into FC1 if possible.
  - Align M7 by minimizing the number of interference fringes on the beam profile at CCD2.
- Before proceeding, check that the focus on CCD1 is in order.
- Use M5 and M6 to align the beam on the vacuum viewport (with the objective removed):
  - Adjust the position on the viewport with M5 visually, e.g., with a diaphragm.
  - Adjust the angle interferometrically with M6 by minimizing the interference pattern at CCD2. Note that the pattern will be very faint as the viewport has an antireflection coating.
  - Lock M5 and M6.

- Insert the objective and align it with the Newport 5-axis mount (LP-2A):
  - Center the objective on the beam.
  - Adjust the angle of the objective interferometrically: Place a dichroic mirror on the rim of the casing of the objective with the 1064nm reflective part towards the objective. Optimize the interference pattern on CCD2
  - Lock the Newport mount carefully while checking the interference pattern.

C Lookup table generation

The following MATLAB code generates a lookup table for the mixer values if provided with a efficiency measurement. It converts the raw measurement data into a format compatible with LabVIEW and removes duplicate data.

```
%%
cd('//jochim-server/allgemeines/AFM_Setup/RF/AOD&RF_efficiency/autorun_
    VCO_sweep_mixer_step_high_res')
A=importdata('z_new_mt_VCO_mixer_realx.adc');
firstrun=0;
%%
makeplots=1;
%%
VCOsteps=8;
VCOstepvoltage=1;                       % in V
VCOsweepvoltage=2;                      % height of ramp in V
timestep=1;                             % in ms
sweeptimestep=5;                        % in ms
sweepstarttime=A(1,3);                  % in ms
sweependtime=max(A(:,3))+timestep;
mixerstepvoltage=0.5;                   % in V
minmixervoltage=0;                      % in V
maxmixervoltage=10;                     % in V
mixersteps=20;
%%
% delete the first column where the recorded ADC_FIFO channels are
% indicated
if firstrun==0
A(:,1)=[];
firstrun=1;
end;
%%
% calculate the VCO voltages from the image number (first column) and
    the
% time (second column).
% NOTE: Check first that the file starts where the autorun actually
% started!
% NOTE: This gives the VCO voltage with the resolution of the ADC FIFO
% measurement step sizes which is not the actual resolution of the VCO
% sweep.
A(:,5)=mod((A(:,1)-A(1,1)),VCOsteps+1).*VCOstepvoltage+(A(:,2)-
    sweepstarttime).*VCOsweepvoltage./(sweependtime-sweepstarttime);
%%
% calculate the mixer voltages
A(:,6)=floor((A(:,1)-A(1,1))./(VCOsteps+1)).*mixerstepvoltage;
%%
```

```
% remove rows where mixer voltage > maximum specified value from
    autorun
A(find(A(:,6)>maxmixervoltage),:)=[];
%%
% round VCO voltage to 1e-4
A(:,5)=round(A(:,5)*1e4)/1e4;
%%
% average the values in blocks of sweeptimestep/timestep
A(:,7)=filter(ones(1,sweeptimestep/timestep)/(sweeptimestep/timestep)
    ,1,A(:,4));
Amean=[A(1:5:end,5) A(1:5:end,6) A(5:5:end,7)];
%%
% remove rows where the VCO voltage is repeated for same mixer voltage
[b,m,n]=unique(Amean(:,1:2),'rows','first');
Bmean=Amean(m,:);
Bmean2=sortrows(Bmean, 2);
%%
% normalize efficiency/PD voltage
nbins=2000;
maxeff=max(Bmean(:,3));
Bmean(:,3)=round(Bmean(:,3)/maxeff*nbins);
maxeff=max(Bmean2(:,3));
Bmean2(:,3)=Bmean2(:,3)/maxeff;
%%
% make a matrix with axes VCO voltage and efficiency and entries mixer
% voltage
ysize=length(unique(Bmean(:,1)));
xsize=nbins;
M=zeros(ysize,xsize);

for n=1:length(Bmean(:,1))
    M(round((Bmean(n,1)*1000)+1),round(Bmean(n,3)))=Bmean(n,2);
end;
%%
% make the interpolation matrix N
ysizeN=length(unique(Bmean2(:,2)));
xsizeN=length(Bmean2(:,1))/ysizeN;
N=zeros(ysizeN,xsizeN);

for p=1:ysizeN
    N(p,1:xsizeN)=Bmean2((p-1)*xsizeN+1:p*xsizeN,3);
end;
%%
% interpolated mixer voltage for a given VCO voltage and "efficiency"
cd('//jochim-server/allgemeines/AFM_Setup/RF/AOD&RF_efficiency');
for q=1:xsize
    for r=1:ysize
        M(r,q)=interpolate(N,r,(q-1)/nbins);
    end
end;
%%
Msingle=single(M);
```

```
%%
dlmwrite('lookuptablesmall.txt',M(1:5:end,:),'delimiter','\t', '
    precision', 6);
```

This lookup table is used by LabVIEW to interpolate the settings for the RF power for any desired efficiency and frequency. The LabVIEW sub-VI is shown in figure C.1. It manipulates the timing table for the ADWin which sets the control voltages for the experiment at the given times. The line containing the desired efficiency is extracted from this table and replaced by the interpolated control voltage values for the mixers.

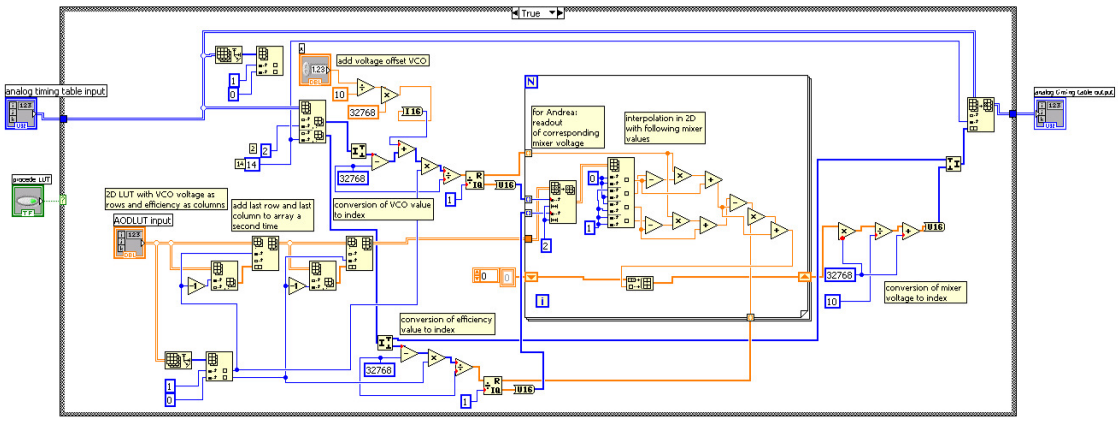

Figure C.1: LabVIEW sub-VI for interpolating the mixer voltages.

D Lists

D.1 List of Figures

2.1 Scattered radial wavefunction for a box potential. 6
2.2 Principle of a Feshbach resonance. 7
2.3 Zeeman hyperfine levels of the ground state of ^{6}Li. 9
2.4 Vacuum system of the experiment. 10
2.5 Intensity profile of the microtrap. 11
2.6 Occupation probability for fermions. 12
2.7 Schematic of the current objective. 14

3.1 Occupation ρ vs. chemical potential μ. 18
3.2 Eigenenergies of one spin $\uparrow$ and one $\downarrow$ particle in a double well. 20
3.3 Eigenenergies of the Hubbard model with off-site interaction in dependence of the barrier height between the sites. 22
3.4 Intensity profiles and position of the extrema for two overlapping Gaussian foci. 23
3.5 Potentials, energy levels and wavefunctions for a double well. 24
3.6 Numerical results for the parameters of the Hubbard model. 25

4.1 Schematic of the breadboard of the new setup. 28
4.2 Schematic of the Michelson interferometer with one spherical mirror. 30
4.3 Wavefront measurements with the interferometer of the objectives. . . 31
4.4 Tests of the focus. 31
4.5 Point spread functions of a pinhole. 32

5.1 Reflection of a optical plane wave on a periodically inhomogeneous medium. 36
5.2 Theoretical intensity reflectance of the AOD. 38
5.3 Bragg condition for the first diffraction order. 40
5.4 RF setup of the control loop for the power stabilization of the laser. . 41
5.5 RF setup for driving the AOD and RF monitoring setup. 42
5.6 RF signal stability. 43
5.7 Calibration of diffraction angle and VCO frequency. 44
5.8 Attenuation of the mixer and measured diffraction efficiency of the AOD. 45
5.9 Frequency response of the AOD. 46
5.10 Grey scale image of four foci. 47
5.11 Lookup table for the AOD. 47

5.12 Frequency response of the AOD with the lookup table. 48

B.1 Schematic of the new setup. 61

C.1 LabVIEW sub-VI for interpolating the mixer voltages. 67

D.2 List of Tables

3.1 Dimensionality, states and Hamiltonians of the subspaces of the 2-site Hubbard model. 19

4.1 Design parameters of the objective from [Ser11a]. 30
4.2 Resolution of objective 'BA1002'. 32

E Bibliography

[Blo29] F. Bloch, *Über die Quantenmechanik der Elektronen in Kristallgittern*, Zeitschrift für Physik A Hadrons and Nuclei **52**, 555–600 (1929).

[Blo08] I. Bloch, J. Dalibard, W. Zwerger, *Many-body physics with ultracold gases*, Rev. Mod. Phys. **80**(3), 885 (2008).

[Chi10] C. Chin, R. Grimm, P. Julienne, E. Tiesinga, *Feshbach resonances in ultracold gases*, Rev. Mod. Phys. **82**, 1225–1286 (2010).

[CVI09] CVI Melles-Griot, *Technical Guide*, https://www.cvimellesgriot.com/Products/Documents/TechnicalGuide/Gaussian-Beam-Optics.pdf (2009).

[Dav95] K. B. Davis, M.-O. Mewes, M. R. Andrews, N. J. van Druten, D. S. Durfee, D. M. Kurn, W. Ketterle, *Bose-Einstein condensation in a gas of sodium atoms*, Phys. Rev. Lett. **75**(22), 3969–3973 (1995).

[Dua05] L.-M. Duan, *Effective Hamiltonian for Fermions in an Optical Lattice across a Feshbach Resonance*, Phys. Rev. Lett. **95**, 243202 (2005).

[Esc75] H. Eschler, F. Weidinger, *Acousto - optic properties of dense flint glasses*, Journal of Applied Physics **46**(1), 65–70 (1975).

[Eve10] J. Evers, *Light-matter interactions*, lecture notes and private correspondence (2010).

[Fey82] R. Feynman, *Simulating physics with computers*, International Journal of Theoretical Physics **21**, 467–488 (1982).

[Gre02] M. Greiner, O. Mandel, T. Esslinger, T. W. Hänsch, I. Bloch, *Quantum phase transition from a superfluid to a Mott insulator in a gas of ultracold atoms*, Nature (London) **415**(6867), 39–44 (2002).

[Gri00] R. Grimm, M. Weidemüller, Y. B. Ovchinnikov, *Optical dipole traps for neutral atoms*, Adv. At. Mol. Opt. Phys. **42**, 95–170 (2000).

[Hec77] D. L. Hecht, *Multifrequency Acoustooptic Diffraction*, IEEE Transactions on Sonics and Ultrasonics **SU-24**, 7–18 (1977).

[Hub63] J. Hubbard, *Electron Correlations in Narrow Energy Bands*, Proceedings of the Royal Society of London. Series A, Mathematical and Physical Sciences **276**(1365), pp. 238–257 (1963).

[Jör08] R. Jördens, N. Strohmaier, K. Gunter, H. Moritz, T. Esslinger, *A Mott insulator of fermionic atoms in an optical lattice*, Nature **455**(7210), 204–207 (2008).

[Jör10] R. Jördens, L. Tarruell, D. Greif, T. Uehlinger, N. Strohmaier, H. Moritz, T. Esslinger, L. De Leo, C. Kollath, A. Georges, V. Scarola, L. Pollet, E. Burovski, E. Kozik, M. Troyer, *Quantitative Determination of Temperature in the Approach to Magnetic Order of Ultracold Fermions in an Optical Lattice*, Phys. Rev. Lett. **104**, 180401 (2010).

[Kes09] J. P. Kestner, *Effective Single-Band Hamiltonians for Strongly Interacting Ultracold Fermions in an Optical Lattice*, Dissertation, University of Michigan (2009).

[Lom11] T. Lompe, *Efimov Physics in a three-component Fermi gas*, Dissertation, University of Heidelberg (2011).

[McK11] D. C. McKay, B. DeMarco, *Cooling in strongly correlated optical lattices: prospects and challenges*, Reports on Progress in Physics **74**(5), 054401 (2011).

[Mer98] E. Merzbacher, *Quantum Mechanics* (John Wiley & Sons, Inc., 1998).

[Mes65] A. Messiah, *Quantum mechanics*, Vol. 1 of *Quantum Mechanics* (1965).

[Met99] H. J. Metcalf, P. van der Straten, *Laser Cooling and Trapping* (Springer-Verlag, New York, 1999).

[Ott10] T. B. Ottenstein, *Few-body physics in ultracold Fermi gases*, Dissertation, University of Heidelberg (2010).

[Qid91] Z. Qida, H. Taiyi, C. Fengyi, D. Xiaoyi, S. Qiuqin, Z. Jianzhong, *Multiple dimensional acousto-optic diffraction and multiple dimensional acousto-optic device*, Shengxue Xuebao **16**, 450–457 (1991).

[Sal91] B. E. A. Saleh, M. C. Teich, *Fundamentals of Photonics* (John Wiley & Sons, Inc., 1991).

[Sca05] V. W. Scarola, S. Das Sarma, *Quantum Phases of the Extended Bose-Hubbard Hamiltonian: Possibility of a Supersolid State of Cold Atoms in Optical Lattices*, Phys. Rev. Lett. **95**, 033003 (2005).

[Sca07] R. Scalettar, *Elementry Introduction to the Hubbard Model*, lecture notes (2007).

[Sch08] U. Schneider, L. Hackermüller, S. Will, T. Best, I. Bloch, T. A. Costi, R. W. Helmes, D. Rasch, A. Rosch, *Metallic and Insulating Phases of Repulsively Interacting Fermions in a 3D Optical Lattice*, Science **322**(5907), 1520–1525 (2008).

[Ser07] F. Serwane, *The setup of a Magneto Optical Trap for the preparation of a mesoscopic degenerate Fermi gas*, Diploma thesis (2007).

[Ser11a] F. Serwane, *Deterministic preparation of a tunable few-fermion system*, Dissertation, University of Heidelberg (2011).

[Ser11b] F. Serwane, G. Zürn, T. Lompe, T. B. Ottenstein, A. N. Wenz, S. Jochim, *Deterministic Preparation of a Tunable Few-Fermion System*, Science **332**(6027), 336–338 (2011).

[Tro08] S. Trotzky, P. Cheinet, S. Fölling, M. Feld, U. Schnorrberger, A. M. Rey, A. Polkovnikov, E. A. Demler, M. D. Lukin, I. Bloch, *Time-Resolved Observation and Control of Superexchange Interactions with Ultracold Atoms in Optical Lattices* **319**(5861), 295–299 (2008).

[Wan37] G. H. Wannier, *The Structure of Electronic Excitation Levels in Insulating Crystals*, Phys. Rev. **52**, 191–197 (1937).

Erklärung:

Ich versichere, dass ich diese Arbeit selbstständig verfasst habe und keine anderen als die angegebenen Quellen und Hilfsmittel benutzt habe.

Heidelberg, den 12.10.2012 .....